Convergence Characteristics of Geometrically Accurate Spatial Finite Elements

Brian Tinsley
Department of Mechanical and
Industrial Engineering,
University of Illinois at Chicago,
Chicago, IL 60607
e-mail: btinsle2@uic.edu

Ahmed A. Shabana
Department of Mechanical and
Industrial Engineering,
University of Illinois at Chicago,
Chicago, IL 60607
e-mail: shabana@uic.edu

The convergence characteristics of three geometrically accurate spatial finite elements (FEs) are examined in this study using an eigenvalue analysis. The spatial beam, plate, and solid elements considered in this investigation are suited for both structural and multibody system (MBS) applications. These spatial elements are based on geometry derived from the kinematic description of the absolute nodal coordinate formulation (ANCF). In order to allow for an accurate reference-configuration geometry description, the element shape functions are formulated using constant geometry coefficients defined using the position-vector gradients in the reference configuration. The change in the position-vector gradients is used to define a velocity transformation matrix that leads to constant element inertia and stiffness matrices in the case of infinitesimal rotations. In contrast to conventional structural finite elements, the elements considered in this study can be used to describe the initial geometry with the same degree of accuracy as B-spline and nonuniform rational B-spline (NURBS) representations, widely used in the computer-aided design (CAD). An eigenvalue analysis is performed to evaluate the element convergence characteristics in the case of different geometries, including straight, tapered, and curved configurations. The frequencies obtained are compared with those obtained using a commercial FE software and analytical solutions. The stiffness matrix is obtained using both the general continuum mechanics (GCM) approach and the newly proposed strain split method (SSM) in order to investigate its effectiveness as a locking alleviation technique. [DOI: 10.1115/1.4048731]

Keywords: absolute nodal coordinate formulation, floating frame of reference formulation, spatial beam elements, spatial plate element, spatial solid element, infinitesimal-rotation finite elements, multibody systems, structural systems

1 Introduction

Use of computer-aided engineering (CAE) in industry *durability investigations* has grown significantly over the last several decades. The application of CAE techniques in the design, analysis, and performance evaluation is necessary for efficient and economic product development as well as accurate and reliable strength calculations. More reliance on credible *virtual prototyping* techniques will eventually lead to less reliance on the costly, time-consuming, and error-prone physical prototyping and experimentation. Nonetheless, the CAE procedures currently used by the automotive, aerospace, and machine industries are based on computer-aided design (CAD)/finite element (FE) technology that suffers from serious limitations, particularly, when converting the CAD solid models to FE analysis meshes. This, in turn, makes industry durability investigations less credible because of the inconsistency between the descriptions used to create the solid models and analysis meshes.

In durability investigations, reduced-order models are often developed for flexible components that have infinite number of degrees-of-freedom [1–7]. Commercial FE software, widely used by the industry, however, often employ elements that cannot correctly represent complex geometries. These elements have displacement fields that are not related by a linear mapping to the computational geometry methods, making the conversion of CAD solid models to FE analysis meshes an iterative process [8]. In the FE literature, both straight and curved elements as well as plate and shell elements are based on different kinematic descriptions and are treated differently in the conventional FE analysis [9–17]. Because of such geometric limitations, the conversion of solid models to FE meshes used for developing the reduced-order models is a costly, error-prone, and time consuming process as evident by the cost of $600 m/year to the U.S. automotive industry alone [18].

The development of reduced-order models is necessary for the analysis of both structural and multibody system (MBS) applications. In the case of *structural analysis*, the system components do not experience finite rigid body displacements, and the inertia matrix in this case remains constant. In MBS applications, on the other hand, the system components undergo large rigid-body displacements including finite rotations. In the case of small deformations, the *floating frame of reference* (FFR) approach is often used to create a local linear problem that allows for systematically reducing the number of coordinates by using component-mode synthesis techniques. Using the consistent rotation-based formulation, new geometrically accurate absolute nodal coordinate formulation (ANCF)/FFR finite elements that can be used for both structural and MBS applications can be developed [19,20]. While these ANCF/FFR elements have a much smaller number of degrees of degrees-of-freedom, they preserve many of the important features of ANCF elements, including accurate description of the geometry in the reference configuration, no distinction made

between the shape functions of plates and shells or straight and curved structures, and consistency with computational geometry methods. The main goal of this study is to evaluate the convergence characteristics of spatial ANCF/FFR beam, plate, and solid elements [21]. To this end, an eigenvalue analysis is performed and the results obtained are compared with the results obtained using a commercial FE software.

2 Scope and Contributions

Developing geometrically accurate and efficient reduced-order models is necessary for increasing reliance on virtual prototyping and testing, regardless of the area of application [22–34]. The goal of this study is to address this challenge by evaluating the convergence characteristics of new spatial ANCF/FFR beam, plate, and solid elements that can be used to develop geometrically accurate reduced-order models in a wide class of engineering applications [21]. The specific contributions of this investigation can be summarized as follows:

(1) Details of the formulation of new infinitesimal-rotation spatial ANCF/FFR beam, plate, and solid elements, that can be used in a wide range of engineering applications, are reviewed.
(2) The formulations of the stiffness matrices using the *general continuum mechanics* (GCM) approach and the newly proposed *strain split method* (SSM) is presented. The SSM effectiveness in the locking alleviation when spatial ANCF/ FFR elements are used is evaluated.
(3) It is shown that, unlike conventional finite elements, the ANCF/FFR formulation makes no distinction between plates and shells, or initially straight or curved geometries because the same shape functions are used for both straight and curved elements. This is achieved by defining the displacement field in terms of constant geometric coefficients obtained using the ANCF position-vector gradients that describe the reference-configuration geometry.
(4) In the numerical investigation performed in this study, three mesh structures are considered; a straight beam with constant cross-section, a straight beam with tapered cross-section, and a curved quarter-circle beam with constant cross-section. It is shown that the geometry can be accurately captured using few elements, whereas a large number of conventional elements is required to approximate the same geometry.
(5) An *eigenvalue analysis* is performed to evaluate the *convergence characteristics* of the three spatial ANCF/FFR elements. The frequencies obtained are compared with the analytical solutions when applicable, and with the frequencies predicted by a commercial FE software. The effect of the locking on the convergence rates and the SSM effectiveness in the locking alleviation are discussed.

When using infinitesimal-rotation finite elements, it is important to distinguish between the FFR and the corotational formulations. In the corotational formulation, a frame is introduced for each element and the frame kinematics is defined by the element nodal coordinates. If infinitesimal rotations are used as element coordinates, the kinematic equations are automatically linearized, a rigid-body motion does not produce zero strains, and the rigid-body inertia cannot be modeled exactly [35,36]. In the FFR formulation, on the other hand, a frame is introduced for the entire body and not for each element separately. The large displacement of this frame is described using Cartesian coordinates and finite rotation parameters. Therefore, the rigid-body kinematics is not linearized regardless of the type of coordinates used for the finite elements, a rigid-body motion leads to zero strains, and exact modeling of the rigid-body inertia can be obtained. Furthermore, the concept of the reference conditions, which is fundamental in the body-based FFR formulation, is not used with the element-based corotational formulation.

The organization of the paper is as follows: in Sec. 3, the geometry configurations of an ANCF mesh are described, and the inertia forces, stress forces, and velocity transformation matrix that defines the ANCF position-vector gradients in terms of consistent rotation-based formulation finite rotations are developed. The MBS equations of motion are also presented. Section 3 also discusses the infinitesimal-rotation assumption of FFR elements and the transformation from finite rotation coordinates to infinitesimal rotations. The three finite elements used in this investigation—the spatial ANCF/FFR beam, plate, and solid elements—are described in Sec. 4. Section 5 describes two methods for obtaining the tangent stiffness matrix; the GCM approach and the newly proposed SSM approach which can be used for locking alleviation. Section 6 describes the three mesh types considered in this investigation. The results of the eigenvalue analysis are presented in Sec. 7, and a summary and conclusions are provided in Sec. 8.

3 ANCF/FFR Element Geometry

In this section, the general procedure used to develop the small-deformation ANCF/FFR finite elements using the ANCF displacement fields is reviewed in order to understand the details of the shape function matrices and to highlight the main assumptions employed in developing these small-deformation elements. The ANCF position-vector gradients play three fundamental roles in developing the new ANCF/FFR elements; (1) to accurately define the geometry in the reference configuration; (2) to define a velocity transformation that allows writing the gradient coordinates in terms of the infinitesimal rotation coordinates; and (3) to define constant geometric coefficients that define a new class of element *displacement shape function matrices* capable of capturing complex geometries and describing correctly rigid body displacements.

3.1 Reference-Configuration Geometry.
Three different configurations are used in order to account for the effect of the initially curved geometry [36]. The *straight configuration*, defined by the parameters $\mathbf{x} = \begin{bmatrix} x_1 & x_2 & x_3 \end{bmatrix}^T$, is used for the convenience of performing the integrations to determine the element inertia and elastic forces. The *curved stress-free reference configuration*, defined by the parameters $\mathbf{X} = \begin{bmatrix} X_1 & X_2 & X_3 \end{bmatrix}^T$, is used to define the actual initial geometry of the element before the load application. If the element is not curved, the straight configuration is the same as the reference configuration. The *current* or *deformed configuration*, defined by the vector $\mathbf{r} = \begin{bmatrix} r_1 & r_2 & r_3 \end{bmatrix}^T$. This global position vector $\mathbf{r}$ can be written as $\mathbf{r} = \mathbf{X} + \mathbf{u}$, where $\mathbf{u} = \begin{bmatrix} u_1 & u_2 & u_3 \end{bmatrix}^T$ is the displacement vector. These three configurations can be used to define constant geometric coefficients that allow capturing accurately the reference-configuration geometry. To this end, the matrix of position-vector gradients $\mathbf{J}$ is written as $\mathbf{J} = \partial \mathbf{r}/\partial \mathbf{X} = (\partial \mathbf{r}/\partial \mathbf{x})(\partial \mathbf{x}/\partial \mathbf{X}) = \mathbf{J}_e \mathbf{J}_o^{-1}$, where $\mathbf{J}_e = \partial \mathbf{r}/\partial \mathbf{x}$, $\mathbf{J}_o = \partial \mathbf{X}/\partial \mathbf{x}$, and the matrix $\mathbf{J}_o$ is used as a mapping between the initial stress-free curved geometry and the straight configuration.

3.2 Position Gradients and Finite-Rotation Parameters.
In the FFR formulation, the large reference (rigid-body) rotation is described using finite-rotation parameters. Therefore, the infinitesimal rotations are not used in the definition of the large displacements. For an FE node i, the columns of the matrix of position-vector gradients $\mathbf{J}_e^i = \begin{bmatrix} \mathbf{r}_x^i & \mathbf{r}_y^i & \mathbf{r}_z^i \end{bmatrix}$ are not in general orthogonal or unit vectors, where $\mathbf{r}^i$ is the position vector of node i, and $\mathbf{r}_\alpha^i = \partial \mathbf{r}^i/\partial \alpha$, $\alpha = x, y, z$ are the position-gradient vectors. The matrix $\mathbf{J}_e^i$ can be written as an orthogonal matrix as $\begin{bmatrix} \mathbf{r}_x^i & \mathbf{r}_y^i & \mathbf{r}_z^i \end{bmatrix} = \mathbf{A}^i(\boldsymbol{\theta}^i)$ if the stretch and shear deformations are neglected at the nodes [19,20,37], where $\mathbf{A}^i(\boldsymbol{\theta}^i)$ is an orthogonal matrix that defines the orientation of a nodal coordinate system in terms of the rotation parameters $\boldsymbol{\theta}^i$ [35,38–40]. The initially curved geometry in the reference configuration can be systematically captured

by writing the nodal gradients as $[\mathbf{r}_x^i \quad \mathbf{r}_y^i \quad \mathbf{r}_z^i] = \mathbf{A}^i(\boldsymbol{\theta}^i)\mathbf{J}_o^i$. Differentiating with respect to time yields [19–21]

$$[\dot{\mathbf{r}}_x^i \quad \dot{\mathbf{r}}_y^i \quad \dot{\mathbf{r}}_z^i] = \tilde{\boldsymbol{\omega}}^i[\mathbf{r}_x^i \quad \mathbf{r}_y^i \quad \mathbf{r}_z^i] = [\tilde{\boldsymbol{\omega}}^i\mathbf{r}_x^i \quad \tilde{\boldsymbol{\omega}}^i\mathbf{r}_y^i \quad \tilde{\boldsymbol{\omega}}^i\mathbf{r}_z^i] \quad (1)$$

where $\tilde{\boldsymbol{\omega}}^i = \dot{\mathbf{A}}^i\mathbf{A}^{iT}$. Using this equation, the angular velocity vector $\boldsymbol{\omega}^i$ is defined as $\boldsymbol{\omega}^i = \mathbf{G}^i\dot{\boldsymbol{\theta}}^i$, where $\mathbf{G}^i$ is a matrix function of the orientation parameters [35]. Therefore, Eq. (1) can be rewritten as

$$[\dot{\mathbf{r}}_x^i \quad \dot{\mathbf{r}}_y^i \quad \dot{\mathbf{r}}_z^i] = -[\tilde{\mathbf{r}}_x^i\boldsymbol{\omega}^i \quad \tilde{\mathbf{r}}_y^i\boldsymbol{\omega}^i \quad \tilde{\mathbf{r}}_z^i\boldsymbol{\omega}^i]$$
$$= -[\tilde{\mathbf{r}}_x^i\mathbf{G}^i\dot{\boldsymbol{\theta}}^i \quad \tilde{\mathbf{r}}_y^i\mathbf{G}^i\dot{\boldsymbol{\theta}}^i \quad \tilde{\mathbf{r}}_z^i\mathbf{G}^i\dot{\boldsymbol{\theta}}^i] \quad (2)$$

Using this equation, one can write the following velocity transformation:

$$\begin{bmatrix} \dot{\mathbf{r}}^i \\ \dot{\mathbf{r}}_x^i \\ \dot{\mathbf{r}}_y^i \\ \dot{\mathbf{r}}_z^i \end{bmatrix} = \begin{bmatrix} \mathbf{I} & \mathbf{0} \\ \mathbf{0} & -\tilde{\mathbf{r}}_x^i\mathbf{G} \\ \mathbf{0} & -\tilde{\mathbf{r}}_y^i\mathbf{G} \\ \mathbf{0} & -\tilde{\mathbf{r}}_z^i\mathbf{G} \end{bmatrix} \begin{bmatrix} \dot{\mathbf{r}}^i \\ \dot{\boldsymbol{\theta}}^i \end{bmatrix} \quad (3)$$

where $\mathbf{I}$ and $\mathbf{0}$ are 3×3 identity and null matrices, respectively. Equation (3) can be used to write the time derivatives of the element nodal coordinates $\mathbf{e}$ in terms of the time derivatives of the orientation parameters as $\dot{\mathbf{e}} = \mathbf{B}\dot{\mathbf{p}}$, where $\mathbf{B}$ is an element velocity transformation matrix formed by the nodal coefficient matrix on the right-hand side of Eq. (3), $\mathbf{p} = [\mathbf{p}^{1T} \quad \mathbf{p}^{2T} \quad \cdots \quad \mathbf{p}^{n_n^T}]^T$, n_n is the total number of element nodes, and $\dot{\mathbf{p}}^i = [\dot{\mathbf{r}}^{iT} \quad \dot{\boldsymbol{\theta}}^{iT}]^T$, $i = 1, 2, \ldots, n_n$, is the time derivative of the nodal coordinates which consists of position and rotation parameters. The number of nodes n_n depends on the type of element used; in this study, $n_n = 2$ in the case of a beam element, $n_n = 4$ for a plate element, and $n_n = 8$ for a solid element. The form of the matrix $\mathbf{B}$ and the nodal coordinates for the spatial beam, plate, and solid elements are defined in Sec. 4 of this paper.

3.3 Inertia and Stress Forces.
The position vector of an arbitrary point on an ANCF element can be written as $\mathbf{r}(\mathbf{x}, t) = \mathbf{S}(\mathbf{x})\mathbf{e}(t)$, where $\mathbf{S}$ is the element shape function matrix, $\mathbf{e}$ is the vector of element nodal coordinates, and t is time [36]. The vector of nodal coordinates at node i of a fully parameterized ANCF element includes position and gradient vectors $\mathbf{r}^i$, $\mathbf{r}_x^i$, $\mathbf{r}_y^i$, and $\mathbf{r}_z^i$. The reference configuration is described by $\mathbf{X} = \mathbf{r}(\mathbf{x}, 0) = \mathbf{S}(\mathbf{x})\mathbf{e}_o$, where $\mathbf{e}_o = \mathbf{e}(t = 0)$ is the vector of initial nodal coordinates in the curved stress-free configuration and can be chosen to ensure that the initially curved geometry is defined accurately. The displacement vector of an arbitrary point can be written as $\mathbf{u} = \mathbf{r} - \mathbf{X} = \mathbf{S}(\mathbf{x})(\mathbf{e} - \mathbf{e}_o) = \mathbf{S}\mathbf{e}_d$, where $\mathbf{e}_d = \mathbf{e} - \mathbf{e}_o$ is the vector of element nodal displacements. The velocity and acceleration vectors can be written, respectively, as $\dot{\mathbf{r}} = \mathbf{S}\dot{\mathbf{e}}$ and $\ddot{\mathbf{r}} = \mathbf{S}\ddot{\mathbf{e}}$. The virtual change in the position vector can be written as $\delta\mathbf{r} = \mathbf{S}\delta\mathbf{e}$. Using this equation, the virtual work of the ANCF element inertia forces can be written as $\delta W_i = \int_V \rho\ddot{\mathbf{r}}^T \delta\mathbf{r}dV = (\mathbf{M}\ddot{\mathbf{e}})^T\delta\mathbf{e}$, where ρ and V are, respectively, the mass density and volume in the straight configuration. The constant symmetric ANCF element mass matrix can then be defined as $\mathbf{M} = \int_V \rho\mathbf{S}^T\mathbf{S}dV$.

The elastic forces can be formulated for fully parameterized ANCF elements using a GCM approach and the virtual work of the stress forces $\delta W_s = -\int_V \boldsymbol{\sigma} : \delta\boldsymbol{\varepsilon}|\mathbf{J}_o|dV = \mathbf{Q}_s^T\delta\mathbf{e}$, where $|\mathbf{J}_o|$ is the determinant of $\mathbf{J}_o$, $\mathbf{Q}_s = -\int_V (\boldsymbol{\sigma} : (\partial\boldsymbol{\varepsilon}/\partial\mathbf{e}))^T|\mathbf{J}_o|dV$ is the vector of the element generalized elastic forces, $\boldsymbol{\varepsilon} = (1/2)(\mathbf{J}^T\mathbf{J} - \mathbf{I})$ is the Green–Lagrange strain tensor which can be written as $\boldsymbol{\varepsilon} = (1/2)(\mathbf{J}_o^{-1T}(\mathbf{J}_e^T\mathbf{J}_e)\mathbf{J}_o^{-1} - \mathbf{I})$ upon using the identity $\mathbf{J} = \mathbf{J}_e\mathbf{J}_o^{-1}$, and

$\boldsymbol{\sigma}$ is the second Piola–Kirchhoff stress tensor. The use of this elastic force formulation leads to zero strain in the initial stress-free curved configuration [36,41].

3.4 ANCF/FFR Nonlinear Equations.
The equations of motion of an ANCF element can be written as $\mathbf{M}\ddot{\mathbf{e}} = \mathbf{Q}$, where $\mathbf{M}$ is the element mass matrix and $\mathbf{Q}$ is the vector of nodal forces. Taking the second time derivative of the velocity transformation $\dot{\mathbf{e}} = \mathbf{B}\dot{\mathbf{p}}$, one has $\ddot{\mathbf{e}} = \mathbf{B}\ddot{\mathbf{p}} + \dot{\mathbf{B}}\dot{\mathbf{p}}$. Substituting this equation into the element equations and premultiplying by the transpose of the matrix $\mathbf{B}$, the FE equations can be written in terms of the finite rotation parameters as $\bar{\mathbf{M}}\ddot{\mathbf{p}} = \bar{\mathbf{Q}}$, where $\bar{\mathbf{M}} = \mathbf{B}^T\mathbf{M}\mathbf{B}$ and $\bar{\mathbf{Q}} = \mathbf{B}^T(\mathbf{Q} - \mathbf{M}\dot{\mathbf{B}}\dot{\mathbf{p}})$ [19–21]. Because the infinitesimal rotation assumption has not been made, the element equations are highly nonlinear and are not suited for developing reduced-order models.

3.5 FFR Formulation and Infinitesimal Rotations.
In the case of small deformations, infinitesimal rotations can be used as nodal coordinates to create a local linear problem that allows for systematically reducing the model dimensionality. For this reason, the FFR formulation is used to create such a local linear problem which is suited for applying component-mode synthesis techniques. Using the FFR approach, the global position vector of a point on a body can be written as $\mathbf{r} = \mathbf{R} + \mathbf{A}_b\bar{\mathbf{r}}_f$, where $\mathbf{A}_b$ is the orthogonal matrix that defines the orientation of the body coordinate system, $\bar{\mathbf{r}}_f$ is the local position vector of the point, and $\mathbf{R}$ is the global position vector of the body reference point. Using the ANCF displacement field, the local position vector $\bar{\mathbf{r}}_f$ can be written as

$$\bar{\mathbf{r}}_f(\mathbf{x}, t) = \mathbf{S}(\mathbf{x})\mathbf{e}(t) = \mathbf{S}(\mathbf{x})\mathbf{e}_o + \mathbf{S}(\mathbf{x})\mathbf{e}_d(t) = \bar{\mathbf{u}}_o(\mathbf{x}) + \bar{\mathbf{u}}_f(\mathbf{x}, t) \quad (4)$$

where $\bar{\mathbf{u}}_o(\mathbf{x}) = \mathbf{S}(\mathbf{x})\mathbf{e}_o$ defines the location of the point before deformation, and $\bar{\mathbf{u}}_f(\mathbf{x}, t) = \mathbf{S}(\mathbf{x})\mathbf{e}_d(t)$ is the deformation vector.

The position-vector gradients at node i can be defined in the case of the FFR formulation as $\mathbf{J}_e^i = [\bar{\mathbf{r}}_{f,x}^i \quad \bar{\mathbf{r}}_{f,y}^i \quad \bar{\mathbf{r}}_{f,z}^i] = \mathbf{J}^i\mathbf{J}_o^i = \mathbf{A}^i(\boldsymbol{\theta}^i)\mathbf{J}_o^i$, where $\bar{\mathbf{r}}_{f,\alpha}^i = \partial\bar{\mathbf{r}}_f^i/\partial\alpha$, $\alpha = x, y, z$. If the small rotation assumption is made, the rotation matrix $\mathbf{A}^i(\boldsymbol{\theta}^i)$ can be written as $\mathbf{A}^i(\boldsymbol{\theta}^i) = \mathbf{I} + \tilde{\boldsymbol{\theta}}^i$, where $\tilde{\boldsymbol{\theta}}^i$ is the skew symmetric matrix associated with the vector $\boldsymbol{\theta}^i$. It follows that $\mathbf{J}_e^i = \mathbf{A}^i(\boldsymbol{\theta}^i)\mathbf{J}_o^i = \mathbf{J}_o^i + \tilde{\boldsymbol{\theta}}^i\mathbf{J}_o^i$. Differentiating this equation with respect to time, one obtains

$$\dot{\mathbf{J}}_e^i = [\dot{\bar{\mathbf{r}}}_{f,x}^i \quad \dot{\bar{\mathbf{r}}}_{f,y}^i \quad \dot{\bar{\mathbf{r}}}_{f,z}^i] = \dot{\tilde{\boldsymbol{\theta}}}^i\mathbf{J}_o^i = \dot{\tilde{\boldsymbol{\theta}}}^i[\mathbf{J}_{o1}^i \quad \mathbf{J}_{o2}^i \quad \mathbf{J}_{o3}^i]$$
$$= -[\tilde{\mathbf{J}}_{o1}^i\dot{\boldsymbol{\theta}}^i \quad \tilde{\mathbf{J}}_{o2}^i\dot{\boldsymbol{\theta}}^i \quad \tilde{\mathbf{J}}_{o3}^i\dot{\boldsymbol{\theta}}^i] \quad (5)$$

where $\mathbf{J}_{o1}^i, \mathbf{J}_{o2}^i$, and $\mathbf{J}_{o3}^i$ are the columns of $\mathbf{J}_o^i$. Therefore, for node i, one can write

$$\begin{bmatrix} \dot{\mathbf{r}}^i \\ \dot{\mathbf{r}}_x^i \\ \dot{\mathbf{r}}_y^i \\ \dot{\mathbf{r}}_z^i \end{bmatrix} = \begin{bmatrix} \mathbf{I} & \mathbf{0} \\ \mathbf{0} & -\tilde{\mathbf{J}}_{o1}^i \\ \mathbf{0} & -\tilde{\mathbf{J}}_{o2}^i \\ \mathbf{0} & -\tilde{\mathbf{J}}_{o3}^i \end{bmatrix} \begin{bmatrix} \dot{\mathbf{r}}^i \\ \dot{\boldsymbol{\theta}}^i \end{bmatrix} \quad (6)$$

This equation can be used to define the velocity transformation $\dot{\mathbf{e}} = \mathbf{B}\dot{\mathbf{p}}$, where the different forms of the velocity transformation matrix $\mathbf{B}$ are defined in Sec. 4 for each element type considered in this study. Equation (6), which shows that the velocity transformation matrix $\mathbf{B}$ is constant in the case of using the infinitesimal rotations and defines $\ddot{\mathbf{e}} = \mathbf{B}\ddot{\mathbf{p}}$, reduces the number of nodal coordinates in the case of fully parameterized ANCF elements from 12 coordinates (three translations and nine gradients) to six

coordinates (three translations and three infinitesimal rotations). Using this velocity transformation, the displacement vector $\mathbf{e}_d$ can be written as $\mathbf{e}_d = \mathbf{B}\mathbf{e}_{rd}$, where $\mathbf{e}_{rd}$ is the element displacement vector, which includes the infinitesimal nodal rotations. Substituting this equation into the equation for $\bar{\mathbf{u}}_f(\mathbf{x}, t)$, one can write $\bar{\mathbf{u}}_f(\mathbf{x}, t) = \mathbf{S}(\mathbf{x})\mathbf{e}_d(t) = \mathbf{S}(\mathbf{x})\mathbf{B}\mathbf{e}_{rd}(t) = \mathbf{S}_d(\mathbf{x})\mathbf{e}_{rd}(t)$, where $\mathbf{S}_d(\mathbf{x}) = \mathbf{S}(\mathbf{x})\mathbf{B}$ is the ANCF/FFR *displacement shape function matrix*, which depends on the elements of the position-gradient matrix $\mathbf{J}_o^i$ that captures accurately the initially curved geometry. These elements, which represent constant geometric coefficients that enter into the definition of $\mathbf{S}_d(\mathbf{x})$, assume the values of zeros and ones for structures with straight geometry.

4 Characterization of Spatial ANCF/FFR Finite Elements

The spatial ANCF/FFR beam, plate, and solid elements can be developed using the displacement field of the fully parameterized ANCF elements [42–44]. Each parent ANCF element is assumed to have 12 degrees-of-freedom per node, including one position and three gradient vectors. The vector of coordinates at node i of the ANCF beam, plate, or solid element can be written as $\mathbf{e}^i = \begin{bmatrix} \mathbf{r}^{iT} & \mathbf{r}_x^{iT} & \mathbf{r}_y^{iT} & \mathbf{r}_z^{iT} \end{bmatrix}^T$, where $\mathbf{r}^i$ is the global position vector of node i and $\mathbf{r}_x^i = \partial \mathbf{r}^i / \partial x$, $\mathbf{r}_y^i = \partial \mathbf{r}^i / \partial y$, and $\mathbf{r}_z^i = \partial \mathbf{r}^i / \partial z$ are the position-vector gradients at the node. The matrix of position-vector gradients $\mathbf{J}_o^i$ that defines the geometry in the initial configuration and the skew-symmetric rotation matrix $\tilde{\boldsymbol{\theta}}^i$ at node i, can be written, respectively, as

$$\mathbf{J}_o^i = \begin{bmatrix} \alpha_{11}^i & \alpha_{12}^i & \alpha_{13}^i \\ \alpha_{21}^i & \alpha_{22}^i & \alpha_{23}^i \\ \alpha_{31}^i & \alpha_{32}^i & \alpha_{33}^i \end{bmatrix}, \quad \tilde{\boldsymbol{\theta}}^i = \begin{bmatrix} 0 & -\theta_3^i & \theta_2^i \\ \theta_3^i & 0 & -\theta_1^i \\ -\theta_2^i & \theta_1^i & 0 \end{bmatrix},$$
$$i = 1, 2, \ldots n_n \tag{7}$$

where n_n is the number of element nodes, θ_1^i, θ_2^i, θ_3^i are the three Euler angles at node i, and α_{kl}^i, $k, l = 1, 2, 3$, are constant geometric coefficients that enter into the definition of the ANCF/FFR element displacement field. The matrix of position-vector gradient $\mathbf{J}_o^i$ is the identity matrix in the special case of an initially straight structure. Using the procedure developed in Sec. 3.5, the nodal displacement-coordinates of the ANCF element can be written in terms of the nodal displacement-coordinates of the ANCF/FFR element as $\mathbf{e}_d = \mathbf{B}\mathbf{e}_{rd}$, where

$$\mathbf{B} = \begin{bmatrix} \mathbf{B}^1 & \mathbf{0} & \cdots & \mathbf{0} \\ \mathbf{0} & \mathbf{B}^2 & \cdots & \mathbf{0} \\ \vdots & \vdots & \ddots & \vdots \\ \mathbf{0} & \mathbf{0} & \cdots & \mathbf{B}^{n_n} \end{bmatrix}, \quad \mathbf{B}^i = \begin{bmatrix} \mathbf{I} & \mathbf{0} \\ \mathbf{0} & -\tilde{\mathbf{J}}_{o1}^i \\ \mathbf{0} & -\tilde{\mathbf{J}}_{o2}^i \\ \mathbf{0} & -\tilde{\mathbf{J}}_{o3}^i \end{bmatrix}, \tag{8}$$
$$i = 1, 2, \ldots n_n$$

The velocity transformation matrix $\mathbf{B}$ is also used to define the displacement shape function matrix $\mathbf{S}_d = \mathbf{S}\mathbf{B}$ in terms of the constant geometric coefficients α_{kl}^i, $k, l = 1, 2, 3$. The shape function matrix $\mathbf{S}_d$ can correctly capture the rigid body modes at the velocity level [37] and can be used to define the element mass matrix as $\mathbf{M} = \int_V \rho \mathbf{S}_d^T \mathbf{S}_d dV$. The specific forms of the displacement shape function matrix $\mathbf{S}_d$ and the velocity transformation matrix $\mathbf{B}$ for the three ANCF/FFR elements are provided in the remainder of this section.

4.1 ANCF/FFR Beam Element. The ANCF/FFR beam element shape functions are developed from those of the spatial ANCF fully parameterized beam element [42]. The ANCF/FFR beam element displacement field is defined in terms of constant

geometric coefficients, which allow for an accurate representation of initially curved geometries. The ANCF shape function matrix can be written as $\mathbf{S}^b = \begin{bmatrix} s_1^b \mathbf{I} & s_2^b \mathbf{I} & \ldots s_8^b \mathbf{I} \end{bmatrix}$, where superscript b refers to beam, the shape functions $s_k^b, k = 1, 2, \ldots 8$, are defined as

$$\left. \begin{aligned} s_1^b &= 1 - 3\xi^2 + 2\xi^3, \quad s_2^b = l^b(\xi - 2\xi^2 + \xi^3), \\ s_3^b &= l^b(\eta - \xi\eta), \quad s_4^b = l^b(\zeta - \xi\zeta), \quad s_5^b = 3\xi^2 - 2\xi^3 \\ s_6^b &= l^b(-\xi^2 + \xi^3), \quad s_7^b = l^b \xi\eta, \quad s_8^b = l^b \xi\zeta \end{aligned} \right\} \tag{9}$$

where $\xi = x/l^b$, $\eta = y/l^b$, $\zeta = z/l^b$, and l^b is the length of the element. The vector of element nodal coordinates is $\mathbf{e}^b = \begin{bmatrix} \mathbf{e}^{b,1T} & \mathbf{e}^{b,2T} \end{bmatrix}^T$, where $\mathbf{e}^{b,i}$ is the vector of nodal coordinates at node i, $i = 1, 2$, which includes position and gradient vectors as defined previously. The nodal displacement-coordinates of the ANCF beam element can be written in terms of the ANCF/FFR nodal displacement-coordinates using the transformation $\mathbf{e}_d^b = \mathbf{B}^b \mathbf{e}_{rd}^b$, where

$$\mathbf{B}^b = \begin{bmatrix} \mathbf{B}^{b,1} & \mathbf{0} \\ \mathbf{0} & \mathbf{B}^{b,2} \end{bmatrix}, \quad \mathbf{B}^{b,i} = \begin{bmatrix} \mathbf{I} & \mathbf{0} \\ \mathbf{0} & -\tilde{\mathbf{J}}_{o1}^{b,i} \\ \mathbf{0} & -\tilde{\mathbf{J}}_{o2}^{b,i} \\ \mathbf{0} & -\tilde{\mathbf{J}}_{o3}^{b,i} \end{bmatrix}, \quad i = 1, 2 \tag{10}$$

The displacement shape function matrix $\mathbf{S}_d^b = \mathbf{S}^b \mathbf{B}^b$ is defined in terms of the constant geometric coefficients $\alpha_{kl}^{b,i}$, $k, l = 1, 2, 3$, as $\mathbf{S}_d^b = \begin{bmatrix} \mathbf{S}_d^{b,1} & \mathbf{S}_d^{b,2} \end{bmatrix}$ [21], where $\mathbf{S}_d^{b,1}$ and $\mathbf{S}_d^{b,2}$ are the shape function submatrices associated, respectively, with the first and second nodes, and are given as $\mathbf{S}_d^{b,1} = \begin{bmatrix} s_1^b \mathbf{I} & -(s_2^b \mathbf{J}_{o1}^{b,1} + s_3^b \mathbf{J}_{o2}^{b,1} + s_4^b \mathbf{J}_{o3}^{b,1}) \end{bmatrix}$ and $\mathbf{S}_d^{b,2} = \begin{bmatrix} s_5^b \mathbf{I} & -(s_6^b \mathbf{J}_{o1}^{b,2} + s_7^b \mathbf{J}_{o2}^{b,2} + s_8^b \mathbf{J}_{o3}^{b,2}) \end{bmatrix}$. In the special case of an initially straight beam where the gradient vectors are $\mathbf{J}_{o1}^{b,i} = \begin{bmatrix} 1 & 0 & 0 \end{bmatrix}^T$, $\mathbf{J}_{o2}^{b,i} = \begin{bmatrix} 0 & 1 & 0 \end{bmatrix}^T$, and $\mathbf{J}_{o3}^{b,i} = \begin{bmatrix} 0 & 0 & 1 \end{bmatrix}^T$, the displacement shape function matrix is $\mathbf{S}_d^b = \begin{bmatrix} s_1^b \mathbf{I} & \tilde{\mathbf{s}}_{\theta 1}^b & s_5^b \mathbf{I} & \tilde{\mathbf{s}}_{\theta 2}^b \end{bmatrix}$, where $\tilde{\mathbf{s}}_{\theta 1}^b$ and $\tilde{\mathbf{s}}_{\theta 2}^b$ are the displacement shape function matrices associated with the nodal rotations in the straight configuration, and are defined as

$$\tilde{\mathbf{s}}_{\theta 1}^b = \begin{bmatrix} 0 & s_4^b & -s_3^b \\ -s_4^b & 0 & s_2^b \\ s_3^b & -s_2^b & 0 \end{bmatrix}, \quad \tilde{\mathbf{s}}_{\theta 2}^b = \begin{bmatrix} 0 & s_8^b & -s_7^b \\ -s_8^b & 0 & s_6^b \\ s_7^b & -s_6^b & 0 \end{bmatrix} \tag{11}$$

These skew-symmetric matrices are associated, respectively, with the vectors $\mathbf{s}_{\theta 1}^b = -\begin{bmatrix} s_2^b & s_3^b & s_4^b \end{bmatrix}^T$ and $\mathbf{s}_{\theta 2}^b = -\begin{bmatrix} s_6^b & s_7^b & s_8^b \end{bmatrix}^T$. The kinematic equations developed for the ANCF/FFR beam element show that the displacement shape function matrix of can be used for both initially straight or curved geometries.

4.2 ANCF/FFR Plate Element. The spatial ANCF/FFR plate element is developed using the displacement field of the fully parameterized spatial ANCF plate element, which has the following shape function matrix and the vector of nodal coordinates [43]:

$$\left. \begin{aligned} \mathbf{S}^p &= \begin{bmatrix} s_1^p \mathbf{I} & s_2^p \mathbf{I} & \ldots & s_{16}^p \mathbf{I} \end{bmatrix} \\ \mathbf{e}^p &= \begin{bmatrix} \mathbf{e}^{p,1T} & \mathbf{e}^{p,2T} & \mathbf{e}^{p,3T} & \mathbf{e}^{p,4T} \end{bmatrix}^T \end{aligned} \right\} \tag{12}$$

In this equation, superscript p refers to plate, and the shape functions $s_i^p, i = 1, 2, \ldots, 16$ are

$$
\begin{aligned}
s_1^p &= (2\xi+1)(\xi-1)^2(2\eta+1)(\eta-1)^2, \quad s_2^p = a^p\xi(\xi-1)^2(2\eta+1)(\eta-1)^2 \\
s_3^p &= b^p\eta(\xi-1)^2(2\xi+1)(\eta-1)^2, \quad s_4^p = t^p\zeta(\xi-1)(\eta-1), \\
s_5^p &= -\xi^2(2\xi-3)(2\eta+1)(\eta-1)^2, \quad s_6^p = a^p\xi^2(\xi-1)(2\eta+1)(\eta-1)^2, \quad s_7^p = -b^p\eta\xi^2(2\xi-3)(\eta-1)^2, \\
s_8^p &= -t^p\xi\zeta(\eta-1), \quad s_9^p = \xi^2\eta^2(2\xi-3)(2\eta-3), \quad s_{10}^p = -a^p\xi^2\eta^2(\xi-1)(2\eta-3), \\
s_{11}^p &= -b^p\xi^2\eta^2(\eta-1)(2\xi-3), \quad s_{12}^p = t^p\xi\eta\zeta, \quad s_{13}^p = -\eta^2(2\xi+1)(\xi-1)^2(2\eta-3), \\
s_{14}^p &= -a^p\xi\eta^2(\xi-1)^2(2\eta-3), \quad s_{15}^p = b^p\eta^2(\xi-1)^2(2\xi+1)(\eta-1), \quad s_{16} = -t^p\eta\zeta(\xi-1)
\end{aligned} \tag{13}
$$

where $\xi = x/a^p$, $\eta = y/b^p$, $\zeta = z/t^p$, a^p, b^p, and t^p are the length, width, and thickness of the element, respectively, and $\mathbf{e}^{p,i}$ is the vector of nodal coordinates, which include position and gradient vectors at node i, $i = 1,2,3,4$. The nodal coordinates of the ANCF plate element can be written in terms of the nodal coordinates of the ANCF/FFR plate element as $\mathbf{e}_d^p = \mathbf{B}^p\mathbf{e}_{rd}^p$, where

$$
\mathbf{B}^p = \begin{bmatrix} \mathbf{B}^{p,1} & \mathbf{0} & \mathbf{0} & \mathbf{0} \\ \mathbf{0} & \mathbf{B}^{p,2} & \mathbf{0} & \mathbf{0} \\ \mathbf{0} & \mathbf{0} & \mathbf{B}^{p,3} & \mathbf{0} \\ \mathbf{0} & \mathbf{0} & \mathbf{0} & \mathbf{B}^{p,4} \end{bmatrix}, \quad \mathbf{B}^{p,i} = \begin{bmatrix} \mathbf{I} & \mathbf{0} \\ \mathbf{0} & -\tilde{\mathbf{J}}_{o1}^{p,i} \\ \mathbf{0} & -\tilde{\mathbf{J}}_{o2}^{p,i} \\ \mathbf{0} & -\tilde{\mathbf{J}}_{o3}^{p,i} \end{bmatrix}, \tag{14}
$$

$$i = 1,2,3,4$$

The displacement shape function matrix $\mathbf{S}_d^p = \mathbf{S}^p\mathbf{B}^p$ is defined in terms of the constant geometric coefficients $\alpha_{kl}^{p,i}$, $k,l = 1,2,3$, as $\mathbf{S}_d^p = \begin{bmatrix} \mathbf{S}_d^{p,1} & \mathbf{S}_d^{p,2} & \mathbf{S}_d^{p,3} & \mathbf{S}_d^{p,4} \end{bmatrix}$ [21], where $\mathbf{S}_d^{p,1}$, $\mathbf{S}_d^{p,2}$, $\mathbf{S}_d^{p,3}$, and $\mathbf{S}_d^{p,4}$ are the shape function matrices associated with the element nodes and are given as

$$
\begin{aligned}
\mathbf{S}_d^{p,1} &= \begin{bmatrix} s_1^p\mathbf{I} & -(s_2^p\mathbf{J}_{o1}^{p,1} + s_3^p\mathbf{J}_{o2}^{p,1} + s_4^p\mathbf{J}_{o3}^{p,1}) \end{bmatrix}, \\
\mathbf{S}_d^{p,2} &= \begin{bmatrix} s_5^p\mathbf{I} & -(s_6^p\mathbf{J}_{o1}^{p,2} + s_7^p\mathbf{J}_{o2}^{p,2} + s_8^p\mathbf{J}_{o3}^{p,2}) \end{bmatrix} \\
\mathbf{S}_d^{p,3} &= \begin{bmatrix} s_9^p\mathbf{I} & -(s_{10}^p\mathbf{J}_{o1}^{p,3} + s_{11}^p\mathbf{J}_{o2}^{p,3} + s_{12}^p\mathbf{J}_{o3}^{p,3}) \end{bmatrix}, \\
\mathbf{S}_d^{p,4} &= \begin{bmatrix} s_{13}^p\mathbf{I} & -(s_{14}^p\mathbf{J}_{o1}^{p,4} + s_{15}^p\mathbf{J}_{o2}^{p,4} + s_{16}^p\mathbf{J}_{o3}^{p,4}) \end{bmatrix}
\end{aligned} \tag{15}
$$

In the special case of an initially straight plate, the gradient vectors are $\mathbf{J}_{o1}^{p,i} = \begin{bmatrix} 1 & 0 & 0 \end{bmatrix}^T$, $\mathbf{J}_{o2}^{p,i} = \begin{bmatrix} 0 & 1 & 0 \end{bmatrix}^T$, and $\mathbf{J}_{o3}^{p,i} = \begin{bmatrix} 0 & 0 & 1 \end{bmatrix}^T$, and the displacement shape function matrix for this plate element can be defined as $\mathbf{S}_d^p = \begin{bmatrix} s_1^p\mathbf{I} & \tilde{\mathbf{s}}_{\theta 1}^p & s_5^p\mathbf{I} & \tilde{\mathbf{s}}_{\theta 2}^p & s_9^p\mathbf{I} & \tilde{\mathbf{s}}_{\theta 3}^p & s_{13}^p\mathbf{I} & \tilde{\mathbf{s}}_{\theta 4}^p \end{bmatrix}$, where $\tilde{\mathbf{s}}_{\theta 1}^p$, $\tilde{\mathbf{s}}_{\theta 2}^p$, $\tilde{\mathbf{s}}_{\theta 3}^p$, and $\tilde{\mathbf{s}}_{\theta 4}^p$ are, respectively, the skew-symmetric matrices associated with the vectors

$$
\begin{aligned}
\mathbf{s}_{\theta 1}^p &= -\begin{bmatrix} s_2^p & s_3^p & s_4^p \end{bmatrix}^T, \quad \mathbf{s}_{\theta 2}^p = -\begin{bmatrix} s_6^p & s_7^p & s_8^p \end{bmatrix}^T \\
\mathbf{s}_{\theta 3}^p &= -\begin{bmatrix} s_{10}^p & s_{11}^p & s_{12}^p \end{bmatrix}^T, \quad \mathbf{s}_{\theta 4}^p = -\begin{bmatrix} s_{14}^p & s_{15}^p & s_{16}^p \end{bmatrix}^T
\end{aligned} \tag{16}
$$

Therefore, the matrix $\mathbf{S}_d^p$ can be used for both initially curved and straight geometries, and there is no need to have a special formulation for shell elements. That is, the geometries of plates and shells can be described using the same displacement field, provided that the constant geometric coefficients $\alpha_{kl}^{p,i}$, $k,l = 1,2,3$, are properly defined.

4.3 ANCF/FFR Solid Element. The shape functions of the three-dimensional ANCF solid element are used as the starting point to define the ANCF/FFR solid element displacement field in terms of constant geometric coefficients [44]. The shape function

matrix and the vector of nodal coordinates of the parent ANCF solid element used in this investigation are defined, respectively, as

$$
\begin{aligned}
\mathbf{S}^s &= \begin{bmatrix} s^{s,1}\mathbf{I} & s^{s,2}\mathbf{I} & s^{s,3}\mathbf{I} & s^{s,4}\mathbf{I} & \cdots & s^{s,29}\mathbf{I} & s^{s,30}\mathbf{I} & s^{s,31}\mathbf{I} & s^{s,32}\mathbf{I} \end{bmatrix} \\
\mathbf{e}^s &= \begin{bmatrix} \mathbf{e}^{s,1T} & \mathbf{e}^{s,2T} & \mathbf{e}^{s,3T} & \mathbf{e}^{s,4T} & \mathbf{e}^{s,5T} & \mathbf{e}^{s,6T} & \mathbf{e}^{s,7T} & \mathbf{e}^{s,8T} \end{bmatrix}^T
\end{aligned} \tag{17}
$$

where superscript s refers to solid and the vector of nodal coordinates at node i is $\mathbf{e}^{s,i}$, $i = 1,\ldots,8$, which includes position and gradient vectors, as defined previously. The shape functions $\mathbf{S}^s$ at node i are defined as

$$
\begin{aligned}
S^{s,1} &= (-1)^{1+\xi_i+\eta_i+\zeta_i}(\xi+\xi_i-1)(\eta+\eta_i-1)(\zeta+\zeta_i-1)\cdot \\
&\quad (1 + (\xi-\xi_i)(1-2\xi) + (\eta-\eta_i)(1-2\eta) + (\zeta-\zeta_i)(1-2\zeta)) \\
S^{s,2} &= (-1)^{\eta_i+\zeta_i}a^s\xi^{\xi_i+1}(\xi-1)^{2-\xi_i}\eta^{\eta_i}(\eta-1)^{1-\eta_i}\zeta^{\zeta_i}(\zeta-1)^{1-\zeta_i} \\
S^{s,3} &= (-1)^{\xi_i+\zeta_i}b^s\xi^{\xi_i}(\xi-1)^{1-\xi_i}\eta^{\eta_i+1}(\eta-1)^{2-\eta_i}\zeta^{\zeta_i}(\zeta-1)^{1-\zeta_i} \\
S^{s,4} &= (-1)^{\xi_i+\eta_i}c^s\xi^{\xi_i}(\xi-1)^{1-\xi_i}\eta^{\eta_i}(\eta-1)^{1-\eta_i}\zeta^{\zeta_i+1}(\zeta-1)^{2-\zeta_i}
\end{aligned}
$$

$$i = 1,2,\ldots,8 \tag{18}$$

where a^s, b^s, and c^s are the dimensions of the element along the axes x,y, and z directions, respectively, $\xi = x/a^s$, $\eta = y/b^s$, $\zeta = z/c^s$, ξ, η, $\zeta \in [0,1]$, and ξ_i, η_i, ζ_i are the dimensionless nodal coordinates of node i. The nodal displacement-coordinates of the ANCF solid element can be written in terms of the nodal displacement-coordinates of the ANCF/FFR solid element as $\mathbf{e}_d^s = \mathbf{B}^s\mathbf{e}_{rd}^s$, where

$$
\mathbf{B}^s = \begin{bmatrix} \mathbf{B}^{s,1} & \mathbf{0} & \cdots & \mathbf{0} \\ \mathbf{0} & \mathbf{B}^{s,2} & \cdots & \mathbf{0} \\ \vdots & \vdots & \ddots & \vdots \\ \mathbf{0} & \mathbf{0} & \cdots & \mathbf{B}^{s,8} \end{bmatrix}, \quad \mathbf{B}^{s,i} = \begin{bmatrix} \mathbf{I} & \mathbf{0} \\ \mathbf{0} & -\tilde{\mathbf{J}}_{o1}^{s,i} \\ \mathbf{0} & -\tilde{\mathbf{J}}_{o2}^{s,i} \\ \mathbf{0} & -\tilde{\mathbf{J}}_{o3}^{s,i} \end{bmatrix}, \quad i = 1,2,\ldots 8 \tag{19}
$$

The displacement shape function matrix $\mathbf{S}_d^s = \mathbf{S}^s\mathbf{B}^s$ is defined in terms of the constant geometric coefficients $\alpha_{kl}^{s,i}$, $k,l = 1,2,3$, as $\mathbf{S}_d^s = \begin{bmatrix} \mathbf{S}_d^{s,1} & \mathbf{S}_d^{s,2} & \ldots & \mathbf{S}_d^{s,8} \end{bmatrix}$ [21], where $\mathbf{S}_d^{s,1}, \mathbf{S}_d^{s,2}, \ldots, \mathbf{S}_d^{s,8}$ are the shape functions associated with the element nodes and are given as

$$
\mathbf{S}_d^{s,k} = \begin{bmatrix} s_{4k-3}^s\mathbf{I} & -(s_{4k-2}^s\mathbf{J}_{o1}^{s,k} + s_{4k-1}^s\mathbf{J}_{o2}^{s,k} + s_{4k}^s\mathbf{J}_{o3}^{s,k}) \end{bmatrix},
$$

$$k = 1,2,\ldots,8 \tag{20}$$

where $\mathbf{S}_d^{s,k}$ are the displacement shape function matrix of the kth node in the element. In the special case of an initially straight solid structure where the gradient vectors are $\mathbf{J}_{o1}^{s,i} = \begin{bmatrix} 1 & 0 & 0 \end{bmatrix}^T$,

$\mathbf{J}_{o2}^{s,i} = \begin{bmatrix} 0 & 1 & 0 \end{bmatrix}^T$, and $\mathbf{J}_{o3}^{s,i} = \begin{bmatrix} 0 & 0 & 1 \end{bmatrix}^T$, the displacement shape function matrix is $\mathbf{S}_d^s = [s_1^s\mathbf{I} \quad \tilde{\mathbf{s}}_{\theta1}^s \quad s_5^s\mathbf{I} \quad \tilde{\mathbf{s}}_{\theta2}^s \quad s_9^s\mathbf{I} \quad \tilde{\mathbf{s}}_{\theta3}^s \quad s_{13}^s\mathbf{I}$ $\tilde{\mathbf{s}}_{\theta4}^s \quad s_{17}^s\mathbf{I} \quad \tilde{\mathbf{s}}_{\theta5}^s \quad s_{21}^s\mathbf{I} \quad \tilde{\mathbf{s}}_{\theta6}^s \quad s_{25}^s\mathbf{I} \quad \tilde{\mathbf{s}}_{\theta7}^s \quad s_{29}^s\mathbf{I} \quad \tilde{\mathbf{s}}_{\theta8}^s]$, where $\tilde{\mathbf{s}}_{\theta1}^s, \tilde{\mathbf{s}}_{\theta2}^s, \ldots, \tilde{\mathbf{s}}_{\theta8}^s$ are the displacement shape functions associated with the nodal rotations in the straight configuration and are defined as

$$\tilde{\mathbf{s}}_{\theta k}^s = \begin{bmatrix} 0 & s_{4k}^s & -s_{4k-1}^s \\ -s_k^s & 0 & s_{4k-2}^s \\ s_{4k-1}^s & -s_{4k-2}^s & 0 \end{bmatrix}, \quad k = 1, 2, \ldots, 8 \qquad (21)$$

where $\tilde{\mathbf{s}}_{\theta k}^s$ is the displacement shape function matrix associated with the rotations of the kth node in the case of the initially straight configuration. Therefore, the matrix $\mathbf{S}_d^s$ can be used for both initially curved and straight geometries.

5 Stiffness Matrix

While there are different methods for formulating the stiffness matrix of the ANCF/FFR elements, the GCM approach is considered in this investigation. Because this approach leads to locking problems in the case of beams and plates, the SSM is used to alleviate the beam and plate Poisson locking [45].

5.1 General Continuum Mechanics Approach. When the stiffness matrix is determined using the GCM approach, the linearized stiffness matrix associated with the ANCF nodal coordinates is first determined using numerical differentiation with respect to the parent ANCF element coordinates. The velocity transformation matrix is then used to obtain the stiffness matrix associated with the ANCF/FFR nodal displacement-coordinates as $\mathbf{K}_d = \mathbf{B}^T\mathbf{K}\mathbf{B}$, where $\mathbf{K}$ is the tangential stiffness matrix of the ANCF element, obtained by differentiating the ANCF elastic force vector with respect to the nodal coordinates as $\mathbf{K} = \partial\mathbf{Q}_s/\partial\mathbf{e}$. The vector of elastic forces $\mathbf{Q}_s$ is determined using the second Piola–Kirchhoff stress tensor $\boldsymbol{\sigma}$ and the Green–Lagrangian strain tensor $\boldsymbol{\varepsilon}$ as explained in Sec. 3.3. The stress and strain tensors $\boldsymbol{\sigma}$ and $\boldsymbol{\varepsilon}$ can be written, respectively, in Voigt form as $\boldsymbol{\sigma}_v = [\sigma_{11} \quad \sigma_{22}$ $\sigma_{33} \quad \sigma_{23} \quad \sigma_{13} \quad \sigma_{12}]^T$ and $\boldsymbol{\varepsilon}_v = [\varepsilon_{11} \quad \varepsilon_{22} \quad \varepsilon_{33} \quad 2\varepsilon_{23} \quad 2\varepsilon_{13} \quad 2\varepsilon_{12}]^T$. Using the stress and strain vectors, the constitutive relation can be written as $\boldsymbol{\sigma}_v = \mathbf{E}\boldsymbol{\varepsilon}_v$, where $\mathbf{E}$ is the matrix of elastic coefficients. The vector of element elastic forces can then be written as $\mathbf{Q}_s = \int_V (\partial\boldsymbol{\varepsilon}_v/\partial\mathbf{e})^T \mathbf{E}\boldsymbol{\varepsilon}_v|\mathbf{J}_o|dV$. The kth column of the tangent stiffness matrix is obtained as $\mathbf{K}_k = (\mathbf{Q}_s(\mathbf{e}_k) - \mathbf{Q}_s(\mathbf{e}_o))/\Delta e_k$, where $\mathbf{e}_o$ is the vector of the ANCF element coordinates in the reference configuration, Δe_k is a perturbation in the kth coordinate, $\mathbf{e}_k = \mathbf{e}_o + \mathbf{b}_k(\Delta e_k)$, and $\mathbf{b}_k$ is a vector with all entries are equal to zero except component b_k which is equal to one. Using the procedure outlined above to determine the stiffness matrix, the initial geometry is correctly captured when calculating the strain tensor because of using $\mathbf{J}_o^{-1}$.

5.2 Locking Alleviation—The Strain Split Method. As in the case of conventional finite elements, in some simulation scenarios, higher order fully parameterized ANCF elements can suffer from locking, including Poisson, shear, volumetric, and curvature locking. The FE locking phenomenon has been an important research topic in the broader FE literature for more than four decades [45]. Several locking-alleviation techniques have been proposed specifically for ANCF elements [46–49]. Because the proposed ANCF/FFR spatial beam and plate elements are based on parent ANCF beam and plate elements, the effect of locking must be considered when developing reduced-order models. For this reason, the newly proposed locking alleviation technique, the SSM is considered in this investigation [45]. This new locking alleviation technique can be applied to both beam and plate elements.

It is important to recognize that there is a fundamental difference between the SSM used in this investigation and the approach used to develop the mixed interpolation of tensorial components (MITC) elements [50,51]. The MITC approach is more related to the mixed variational approaches used in the enhanced assumed strain procedures. In the MITC shell element, the strain fields, derived from the displacement fields of these elements, lead to significant locking, and therefore, modified versions of the strain components are adopted by selecting their interpolation at certain material points on the element; that is, the strain component evaluation is changed. In the SSM approach, on the other hand, the definition of the strain components is not modified; instead, the strain components are simply decomposed and used with a modified constitutive model to define the elastic forces, leading to the locking alleviation. The SSM decomposition of the strain is not dependent on whether small or large deformation problems are considered because the general definition of the Green–Lagrange strain tensor is used in the SSM decomposition, and no components of the infinitesimal strain tensor are used.

6 Geometry Examples Used in This Investigation

Tapered and curved structures are examples of geometries that become distorted and cannot be captured using the kinematic description of conventional structural finite elements, which do not employ position gradients as nodal coordinates from the outset. In this investigation, numerical examples are used to demonstrate use of ANCF/FFR elements for accurate geometry representation. An eigenvalue analysis is performed to evaluate the convergence characteristics of each of the three elements discussed in this paper using three different geometric configurations—a straight uniform thickness structure, a straight structure that is tapered in one direction, and a quarter-circular structure with uniform cross section. The three elements were used to create meshes of the three different geometric configurations for the eigenvalue analysis, resulting in total of nine models. Two elastic force formulations are used to develop the tangential stiffness matrix. For all three elements, the GCM approach is used without locking alleviation technique. The SSM locking-alleviation technique is used to formulate the elastic forces of the beam and plate element meshes only; such a technique is not used with the solid element due to the lack of an element centerline or midsurface. The results obtained are compared with analytical solutions when applicable, as well as the commercial FE software ANSYS [52]. It is important to point out, however, that the ANCF/FFR elements have new shape functions that are fundamentally different from those used for the analytical models and commercial FE software. The ANCF/FFR displacement field defines positions and displacements in a Cartesian coordinate system, while in the analytical approaches, the assumed displacement field is designed using the axial and bending displacements, which are assumed in most models to be uncoupled. Because of the many simplifying assumptions used in developing the analytical models, such models should not always be viewed as the most accurate models; more numerical studies are needed to evaluate their accuracy using new and more general computational techniques that account for the coupling between different displacement modes. This mode coupling may lead to higher stiffness, and therefore, the results obtained using the new elements, if they differ from the results obtained using conventional elements, may require different interpretations and future investigations.

6.1 Straight Beam With Uniform Cross Section. For the straight beam example with uniform cross section, the ANCF/FFR beam, plate, and solid elements are used to construct a mesh with a straight rectangular cross section and simply supported end conditions. Each of the ANCF/FFR meshes are modeled as simply supported with a constant cross-sectional area with height $h = 0.1\,\mathrm{m}$, width $w = 0.1\,\mathrm{m}$, and length $l = 2.0\,\mathrm{m}$. The modulus of elasticity, Poisson ratio, and density of the material chosen are

given, respectively, as $E = 10^9$ Pa, $\nu = 0.3$, and $\rho = 7850\,\text{kg/m}^3$. The material properties are the same for all three structures considered. The eigenvalues obtained using the ANCF/FFR elements are compared with the results obtained using the commercial FE software ANSYS using the BEAM188, SHELL181, and SOLID185 elements, as well as the analytical solution obtained using Timoshenko and Euler–Bernoulli beam theory. For the shell and solid elements, to ensure that the reference conditions are consistent with the reference conditions of the beam element mesh; the plate and solid element meshes have been supported in the middle of the two ends. A two-element wide mesh is used for the shell elements, and a two-by-two cross section mesh is used for the solid elements.

6.2 Straight Beam With Tapered Cross Section. The kinematic description of some conventional FE beam and plate elements can only represent a uniform cross section that cannot be varied along the length of the structure by changing the element nodal coordinates. This leads to the problem of stepped geometry in the event that a tapered structure is being considered. The spatial ANCF/FFR beam and plate elements developed in this investigation are capable of representing linear variation in the thickness, and the plate elements can vary nonlinearly in the width. For this example, a cantilever structure with a tapered cross section thickness, shown in Fig. 1, was developed using the spatial ANCF/FFR beam, plate, and solid elements. The length of the structure is $l = 2.0$ m, and the cross section height varies from $h_1 = 0.2$ m at the left end to $h_2 = 0.1$ m at the right end. The width is assumed constant at $w = 0.1$ m. An eigenvalue analysis was performed on each mesh and the convergence of the first inplane and out-of-plane bending frequencies of each mesh is compared to the ANSYS BEAM188, SHELL181, and SOLID185 elements. A 1000-element BEAM188 mesh is taken as the converged solution and is used as the reference for comparison.

6.3 Curved Beam With Uniform Cross Section. A quarter-circle cantilever beam structure with a uniform cross section and radius $R = 2$ m, shown in Fig. 2, is used as the third numerical example. The curved geometry was chosen to demonstrate the rate of eigenvalue convergence in a geometry that varies nonlinearly. Conventional hexahedral elements use only position coordinates, and do not ensure continuity of the rotations at the nodes. The ANCF/FFR solid element has six degrees-of-freedom per node, including three rotations in addition to the three position coordinates, and therefore, such an element is capable of representing nonlinear variations in surface geometry. Furthermore, the initial geometry of the structure is accurately represented because, as explained in this paper, the ANCF/FFR elements preserve the ANCF reference-configuration geometry, which is related by a linear mapping to the B-spline and NURBS geometries. As with the previous examples, the spatial ANCF/FFR beam, plate, and solid elements are used to model the curved geometry of this example. The results obtained using these elements for the first inplane and out-of-plane bending frequencies are compared with the results obtained using ANSYS BEAM188, SHELL181, and SOLID185 elements. A 1000-element BEAM188 mesh is taken as the converged reference solution.
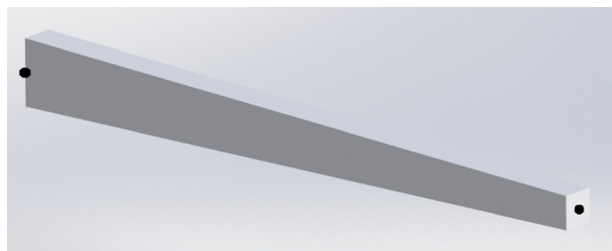
Fig. 1   Tapered beam example

Fig. 2   Curved beam example

7   Numerical Results

In this section, the results of the frequency analysis obtained using the meshes and elements described in the preceding section are discussed.

7.1 Straight Beam With Uniform Cross Section. Table 1 presents a comparison of the results of the first bending frequencies for the straight beam with uniform cross section. The table includes the results of the ANCF/FFR beam, plate, and solid elements for varying mesh refinements, ANSYS BEAM188, SHELL181, and SOLID185 elements for varying mesh refinements, and the analytical solution obtained using Timoshenko and
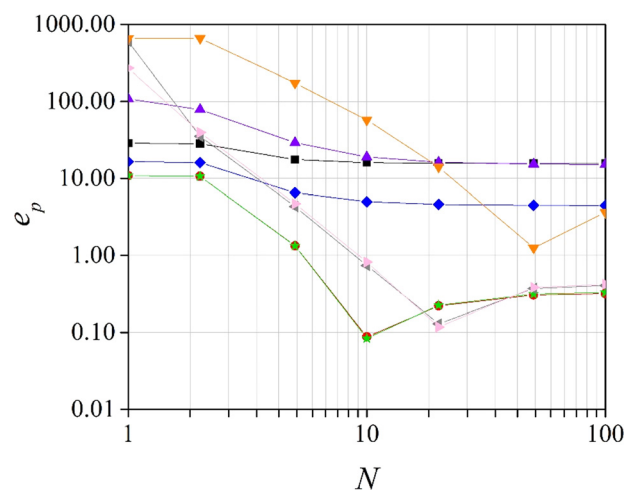
Fig. 3   Error in the first bending frequency of the straight beam (——■—— ANCF/FFR GCM 3D beam, ——●—— ANCF/FFR SSM 3D beam, ——◆—— ANCF/FFR GCM plate, ——★—— ANCF/FFR SSM plate, ——▲—— ANCF/FFR GCM solid, ——◄—— ANSYS BEAM188, ——▶—— ANSYS SHELL181, ——▼—— ANSYS SOLID185)

Table 1 First bending frequency (rad/s) of the straight structure using different formulations

Formulation/number of elements N	1	2	5	10	20	50	100
ANCF/FFR GCM 3D beam	32.7039	32.5999	29.8656	29.4988	29.4081	29.3828	29.3792
ANCF/FFR SSM 3D beam	28.1872	28.1205	25.7609	25.4443	25.3660	25.3441	25.3410
ANCF/FFR GCM plate $N \times 2$	29.5974	29.5003	27.0754	26.6889	26.5905	26.5622	26.5578
ANCF/FFR SSM plate $N \times 2$	28.1869	28.1199	25.7601	25.4433	25.3647	25.3422	25.3388
ANCF/FFR GCM solid $N \times 2 \times 2$	52.8882	45.3150	32.8058	30.2468	29.5383	29.3178	29.2821
ANSYS BEAM188	177.3321 (torsion)	34.3805	26.5193	25.6094	25.3891	25.3279	25.3192
ANSYS SHELL181 $N \times 2$	94.1361 (axial)	35.4760	26.6151	25.6300	25.3921	25.3251	25.3151
ANSYS SOLID185 $N \times 2 \times 2$	191.6296 (torsion)	193.0538	69.6048	40.0467	28.9948	25.1043	24.4991
Euler–Bernoulli				25.422			
Timoshenko				25.315			
1000 element BEAM188				25.3163			

Table 2 Second bending frequency (rad/s) of the straight structure using different formulations

Formulation/number of elements N	1	2	5	10	20	50	100
ANCF/FFR GCM 3D beam	191.6942	130.4098	124.0558	118.0531	116.6132	116.2144	116.1576
ANCF/FFR SSM 3D beam	191.6942	112.3991	107.2571	102.0559	100.8083	100.4627	100.4135
ANCF/FFR GCM plate $N \times 2$	341.9628	121.3376	113.5994	107.2422	105.6727	105.2252	105.1564
ANCF/FFR SSM plate $N \times 2$	341.9629	112.3894	107.2429	102.0397	100.7876	100.4335	100.3791
ANCF/FFR GCM solid $N \times 2 \times 2$	176.6529	138.5419	130.1758	119.6960	116.7695	115.6741	115.4545
ANSYS BEAM188	618.1954 (axial)	164.9812 (torsion)	120.7506	104.7094	101.1722	100.2127	100.0767
ANSYS SHELL181 $N \times 2$	182.7274 (torsion)	122.4986 (shear)	122.8065	105.0510	101.2182	100.1696	100.0143
ANSYS SOLID185 $N \times 2 \times 2$	307.1132 (axial)	284.9385 (axial)	302.6457	162.3752	115.4367	99.4000	96.9092
Euler–Bernoulli				101.689			
Timoshenko				99.966			
1000 element BEAM188				100.0319			

Euler–Bernoulli beam theory. In Table 1 as well as the following tables and figures, N is the number of elements used in the longitudinal direction of the structure. The ANCF/FFR stiffness matrix is evaluated using both the GCM approach and SSM. Figure 3 shows the percentage relative error e_p in the frequencies with respect to Euler–Bernoulli beam theory. In this figure and the following figures discussed in this section, the percentage relative error is calculated using the equation $e_p = (s_m - s_r) \times 100/s_r$, where s_m is the solution obtained using different models, and s_r is
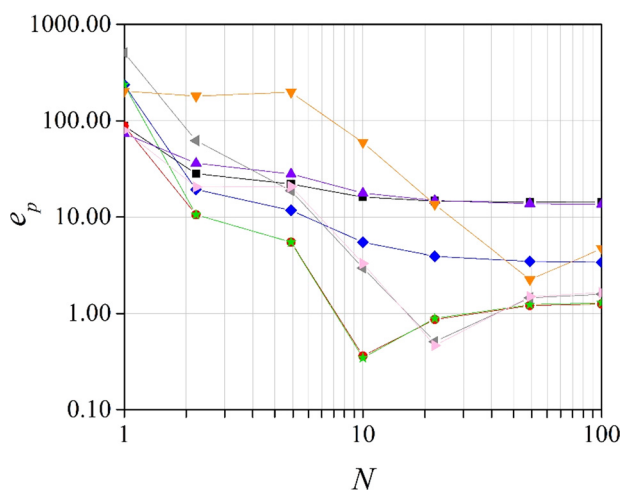
Fig. 4 Error in the second bending frequency of the straight beam (——■——ANCF/FFR GCM 3D beam, ——●——ANCF/FFR SSM 3D beam, ——◆——ANCF/FFR GCM plate, ——★——ANCF/FFR SSM plate, ——▲——ANCF/FFR GCM solid, ——◀——ANSYS BEAM188, ——▶——ANSYS SHELL181, ——▼——ANSYS SOLID185)

the reference solution. Because the ANSYS BEAM188 1000-element solution is in good agreement with Euler–Bernoulli and Timoshenko beam theories, it is used as the converged reference solution for models in which there are no analytical solutions available. Table 2 presents the results of the second bending frequencies for the same meshes, and Fig. 4 shows the percentage relative errors in the frequencies. It can be seen that the GCM meshes converge to a frequency higher than the analytical solution due to the Poisson locking that arises because a higher order polynomial is used in the longitudinal direction compared to the transverse directions [49]. However, the frequencies for the ANCF/FFR SSM beam and plate element models are in good agreement with the analytical solution, demonstrating SSM effectiveness as a locking alleviation technique for beam and plate elements. It is clear that the ANCF/FFR beam and plate SSM models converge faster than the ANSYS BEAM188 and SHELL181 elements. While the ANSYS SOLID185 element does not converge as well as the ANSYS beam and plate elements, it can be noted that the ANSYS SOLID185 mesh with an element aspect ratio closest to one ($N = 50$) results in the closest frequency to the analytical solution. This example demonstrates that the ANCF/FFR elements with the SSM elastic force formulation converge to the correct solution at a faster rate compared to the finite elements implemented in commercial FE software.

7.2 Straight Beam With Tapered Cross Section. Because rotation-based displacement fields of conventional beam and plate finite elements cannot have varying cross section thickness by changing the nodal coordinates, a large number of elements are required to approximate a tapered-structure geometry, leading to a stepped geometry. ANCF/FFR elements, on the other hand, can be used to accurately model a structure with linearly varying thickness, using only a single element, as shown in Fig. 1. Tables 3 and 4 show the first in-plane and out-of-plane bending frequencies for the tapered meshes considered. Figures 5 and 6 show the first

Table 3 First in-plane bending frequency (rad/s) of the tapered structure using different formulations

Formulation/number of elements N	1	2	5	10	20	50	100
ANCF/FFR GCM 3D beam	31.6704	23.7657	22.8707	22.7545	22.7256	22.7175	22.7175
ANCF/FFR SSM 3D beam	27.6221	20.5424	19.7674	19.6667	19.6417	19.6347	19.6337
ANCF/FFR GCM plate $N \times 2$	29.5201	22.3989	21.0271	20.7542	20.6478	20.6004	20.5910
ANCF/FFR SSM plate $N \times 2$	27.6221	20.5424	19.7674	19.6667	19.6417	19.6347	19.6337
ANCF/FFR GCM solid $N \times 2 \times 2$	40.6038	28.0982	23.8727	23.0720	22.8168	22.7137	22.6922
ANSYS BEAM188	14.1649	18.3714	19.4210	19.5370	19.5642	19.5717	19.5727
ANSYS SHELL181 $N \times 2$	18.1454	18.0638	17.3248	17.1712	17.1241	17.1071	17.1041
ANSYS SOLID185 $N \times 2 \times 2$	130.1173	71.4767	33.5133	23.4403	20.0917	19.0314	18.8739
1000 element BEAM188				19.5731			

Table 4 First out-of-plane bending frequency (rad/s) of the tapered structure using different formulations

Formulation/number of elements N	1	2	5	10	20	50	100
ANCF/FFR GCM 3D beam	15.1093	13.3050	12.9364	12.8850	12.8722	12.8686	12.8681
ANCF/FFR SSM 3D beam	13.0301	11.4724	11.1544	11.1101	11.0991	11.0960	11.0955
ANCF/FFR GCM plate $N \times 2$	36.2924	21.0132	15.0312	13.8731	13.5437	13.4346	13.4137
ANCF/FFR SSM plate $N \times 2$	36.2927	21.0131	15.0311	13.8731	13.5438	13.4347	13.4134
ANCF/FFR GCM solid $N \times 2 \times 2$	35.7582	20.6194	14.5825	13.3747	13.0204	12.8989	12.8763
ANSYS BEAM188	9.4597	10.9236	11.0813	11.0884	11.0894	11.0897	11.0897
ANSYS SHELL181 $N \times 2$	8.9538	10.7804	11.0967	11.1179	11.1214	11.1220	11.1220
ANSYS SOLID185 $N \times 2 \times 2$	113.0915	67.3278	29.4375	17.4380	12.7290	11.0473	10.7845
1000 element BEAM188				11.0897			
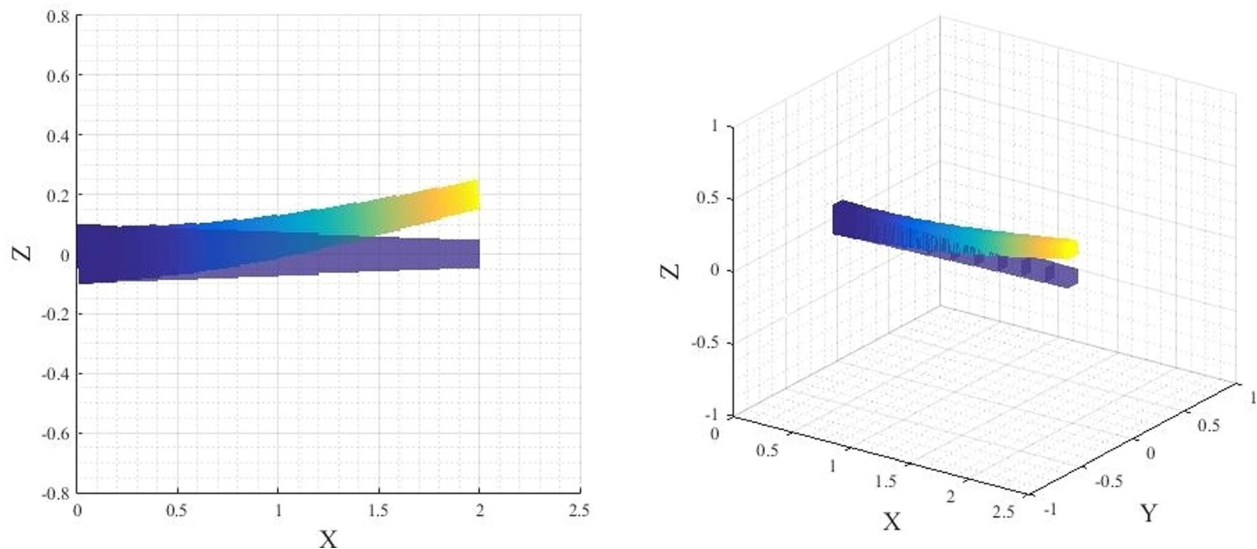
Fig. 5 Multiview of the first in-plane bending mode shape of the tapered beam

in-plane and out-of-plane bending mode shapes of the ANCF/FFR beam model, respectively. The percentage relative frequency errors for the two modes are shown in Figs. 7 and 8. There are fewer data points for the ANSYS BEAM188 curve because the relative error is 0, which cannot be plotted on a log–log plot. The results obtained for the tapered geometry show similar trends compared to the straight-geometry results previously reported; the GCM frequencies converge to a higher value due to the increased stiffness caused by the Poisson locking, and the SSM frequencies converge to the correct solution. Furthermore, the solid element model, which cannot utilize the SSM locking alleviation, converges to a higher natural frequency for both the in-plane and out-of-plane mode shapes. Also as in the case of the straight mesh, the ANSYS SHELL181 and SOLID185 elements converge to a frequency below the correct solution.

It is important to note that the out-of-plane frequencies for the ANCF/FFR plate element are not affected by SSM locking alleviation. This is because the plate midsurface is defined in the lateral plane with respect to the plate, and therefore, vibration must occur across this plane. For the cases of out-of-plane frequencies, the vibration occurs in the same plane as the plate midsurface; therefore, the decomposed strain terms are not properly defined away from the midsurface. However, it is evident that the in-plane plate frequencies for the SSM case converge to the correct solution. Furthermore, both in-plane and out-out-plane frequencies for the ANCF/FFR beam element SSM model converge to the correct value, because the beam centerline is symmetric with respect to both directions of vibration.

7.3 Curved Beam With Uniform Cross Section. As in the case of tapered structures, a relatively large number of conventional finite elements is required to approximate the curved structure geometry as compared to the ANCF/FFR elements. In the
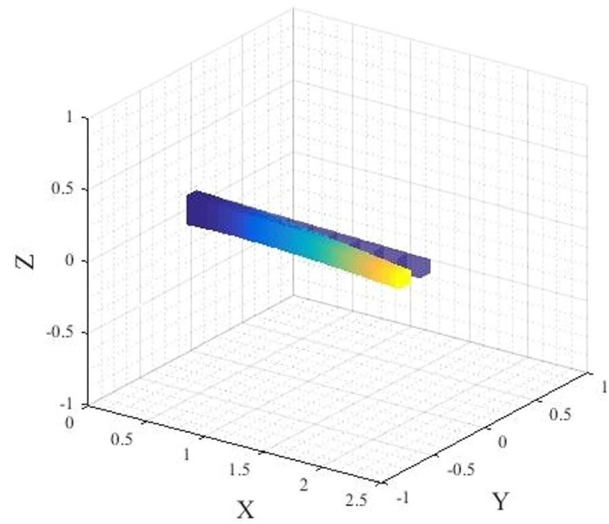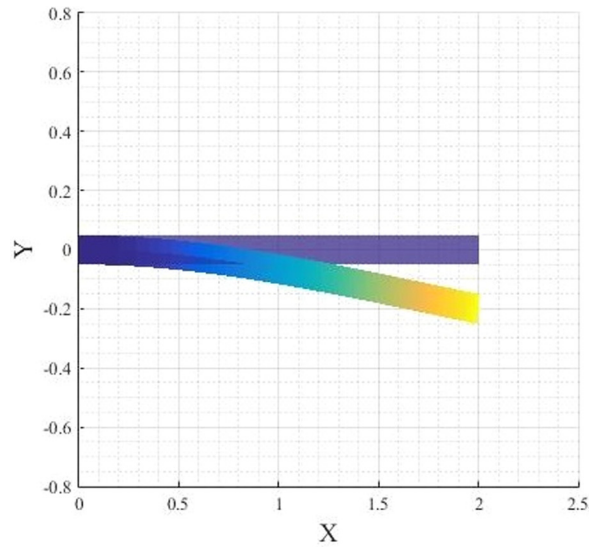
Fig. 6 Multiview of the first out-of-plane bending mode shape of the tapered beam
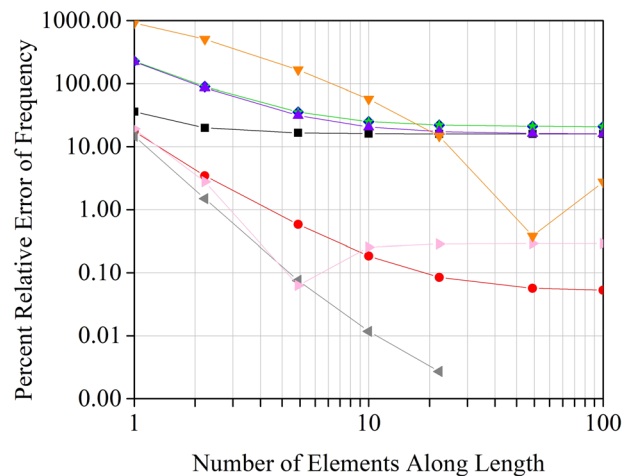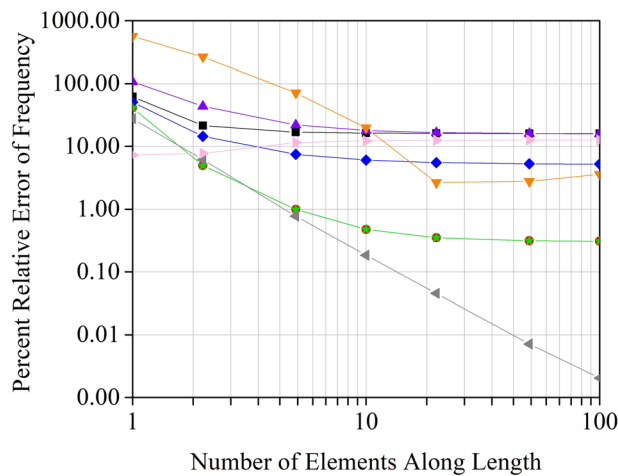
Fig. 7 Error in the first in-plane bending frequency of the tapered beam (──■──ANCF/FFR GCM 3D beam, ──●──ANCF/FFR SSM 3D beam, ──◆──ANCF/FFR GCM plate, ──★──ANCF/FFR SSM plate, ──▲──ANCF/FFR GCM solid, ──◀──ANSYS BEAM188, ──▶──ANSYS SHELL181, ──▼──ANSYS SOLID185)

Fig. 8 Error in the first out-of-plane bending frequency of the tapered beam (──■──ANCF/FFR GCM 3D beam, ──●──ANCF/FFR SSM 3D beam, ──◆──ANCF/FFR GCM plate, ──★──ANCF/FFR SSM plate, ──▲──ANCF/FFR GCM solid, ──◀──ANSYS BEAM188, ──▶──ANSYS SHELL181, ──▼──ANSYS SOLID185)

Table 5 First in-plane bending frequency (rad/s) of the curved structure using different formulations

Formulation/number of elements N	1	2	5	10	20	50	100
ANCF/FFR GCM 3D beam	109.2084	33.9920	6.7518	4.6318	4.4805	4.4736	4.4738
ANCF/FFR SSM 3D beam	73.3045	29.8266	6.3383	4.0607	3.8690	3.8552	3.8547
ANCF/FFR GCM plate $N \times 2$	108.5198	33.1387	6.4425	4.2558	4.0747	4.0547	4.0519
ANCF/FFR SSM plate $N \times 2$	72.5980	29.0768	6.2307	4.0479	3.8676	3.8550	3.8545
ANCF/FFR GCM solid $N \times 2 \times 2$	76.6774	22.4410	6.6824	4.9141	4.5787	4.4885	4.4731
ANSYS BEAM188	4.3211	4.1789	3.9140	3.8706	3.8595	3.8564	3.8560
ANSYS SHELL181 $N \times 2$	4.4720	4.2349	3.9312	3.8796	3.8653	3.8605	3.8596
ANSYS SOLID185 $N \times 2 \times 2$	101.8209	47.2564	16.0330	8.4449	5.2879	3.9992	3.7797
1000 element BEAM188	3.8558						

case of the ANCF/FFR elements, the use of the parent ANCF element, which has position-vector gradients as nodal coordinates, allows modeling the curved-structure geometry shown in Fig. 2 using only two ANCF/FFR elements. Tables 5 and 6 present the

first in-plane and out-of-plane bending frequencies for the curved geometry considered, while Figs. 9 and 10 show the first in-plane and out-of-plane bending mode shapes of the ANCF/FFR beam model, respectively. The percentage relative errors in the

Table 6 First out-of-plane bending frequency (rad/s) of the curved structure using different formulations

Formulation/number of elements N	1	2	5	10	20	50	100
ANCF/FFR GCM 3D beam	25.2684	8.1925	4.7255	4.1991	4.1548	4.1502	4.1499
ANCF/FFR SSM 3D beam	21.0215	7.8382	4.4274	3.7946	3.7419	3.7373	3.7371
ANCF/FFR GCM plate $N \times 2$	32.7246	11.2278	5.6383	4.6904	4.4257	4.3443	4.3314
ANCF/FFR SSM plate $N \times 2$	28.2453	10.9113	5.6282	4.6879	4.4242	4.3430	4.3302
ANCF/FFR GCM solid $N \times 2 \times 2$	26.8680	8.2285	5.1307	4.4407	4.2236	4.1245	4.1017
ANSYS BEAM188	4.3211	4.0611	3.7252	3.6731	3.6599	3.6563	3.6557
ANSYS SHELL181 $N \times 2$	5.1998	4.1273	3.4804	3.3757	3.3458	3.3349	3.3325
ANSYS SOLID185 $N \times 2 \times 2$	95.8833	9.1914	6.9048	5.7906	4.6157	3.8374	3.6819
1000 element BEAM188	3.6556						
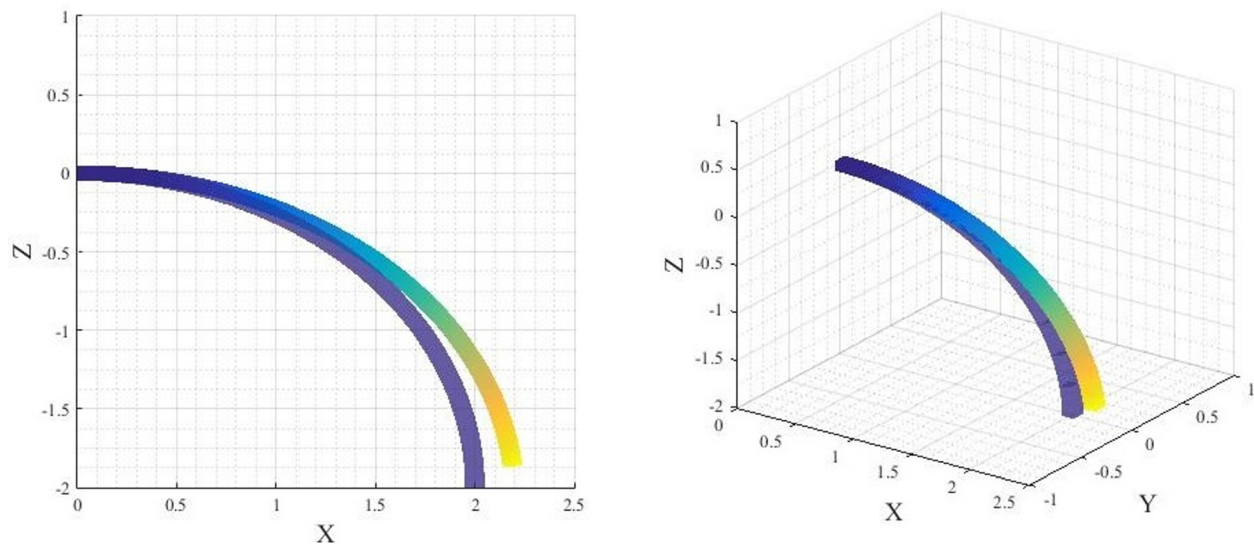
Fig. 9 Multiview of the first in-plane bending mode shape of the curved beam
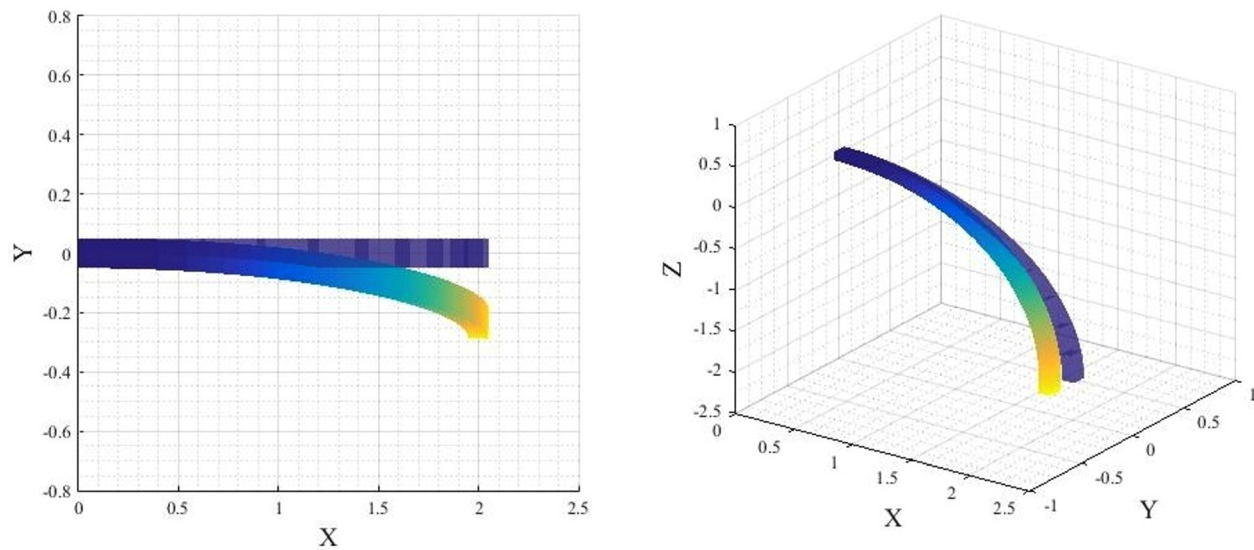
Fig. 10 Multiview of the first out-of-plane bending mode shape of the curved beam

frequencies are shown in Figs. 11 and 12. The results are similar to the previous two cases in that SSM meshes converge to the correct values, except for the out-of-plane modes for the reasons previously explained, and the GCM frequencies are too high due to the Poisson locking effect. The fact that the very coarse ANSYS meshes agree more closely with the correct solution as compared to the ANCF/FFR meshes is a coincidence because the geometry

of this model is not accurately described using conventional element kinematics. This example demonstrates that the ANCF/FFR elements can be used to model initially curved structures without geometry distortion, and demonstrates effectiveness of the SSM locking alleviation technique.

Because locking can lead to deterioration in the computational efficiency and in the element convergence characteristics, the
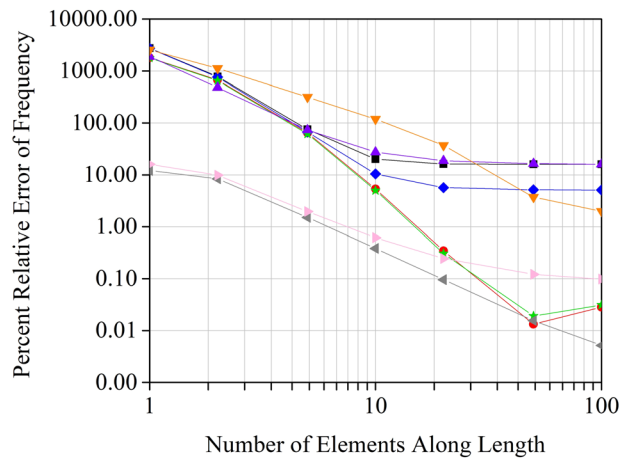
Fig. 11 Error in the first in-plane bending frequency of the curved beam (——■——ANCF/FFR GCM 3D beam, ——●——ANCF/FFR SSM 3D beam, ——◆——ANCF/FFR GCM plate, ——★——ANCF/FFR SSM plate, ——▲——ANCF/FFR GCM solid, ——◄——ANSYS BEAM188, ——▷——ANSYS SHELL181, ——▼——ANSYS SOLID185)
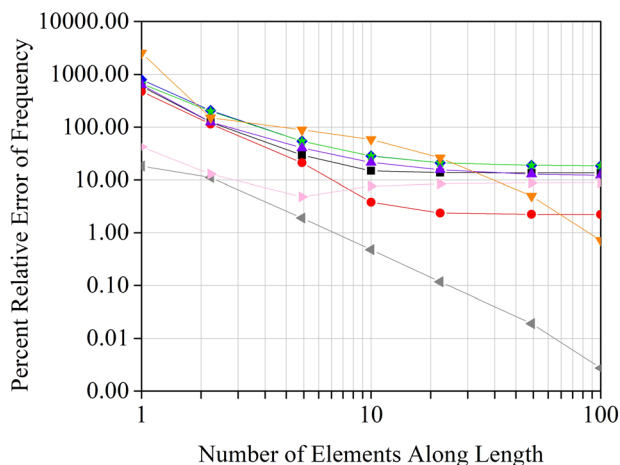
Fig. 12 Error in the first out-of-plane bending frequency of the curved beam (——■——ANCF/FFR GCM 3D beam, ——●——ANCF/FFR SSM 3D beam, ——◆——ANCF/FFR GCM plate, ——★——ANCF/FFR SSM plate, ——▲——ANCF/FFR GCM solid, ——◄——ANSYS BEAM188, ——▷——ANSYS SHELL181, ——▼——ANSYS SOLID185)

SSM locking alleviation technique has proven to be very effective in addressing the locking problem, improving the convergence characteristics, and enhancing the computational efficiency of fully parameterized ANCF elements. Because this paper is focused on the eigenvalue analysis which does not require performing time-dependent dynamic-analysis simulations, the efficiency is not an issue in this study. Nonetheless, the effectiveness of the SSM method in solving the locking problem has been already demonstrated in the literature [45,53].

8 Conclusions

In the classical FE literature, different displacement fields are used for straight and curved elements, and for plate and shell elements. Furthermore, the kinematics of these elements is not linearly related to B-splines and NURBS. Nonetheless, these elements are widely used in industry to create reduced-order models for virtual prototyping and design. Because incompatible methods are currently used in the CAE process for creating the geometry and defining the FE analysis mesh, converting CAD solid models to analysis meshes lacks a scientific foundation, and consequently, is an error-prone process. This paper addresses this fundamental CAE problem by evaluating the convergence characteristics of new geometrically accurate three-dimensional beam, plate, and solid infinitesimal-rotation elements based on the ANCF kinematic description [21]. These elements allow developing geometrically accurate reduced-order models that can be used for both structural and MBS applications. Arbitrary large displacements can be described by using the FFR kinematic description. The initial geometry is described using the ANCF position-vector gradients, which allow modeling complex geometries. The gradients are written in terms of infinitesimal rotations by using a constant velocity transformation matrix. Component-mode synthesis techniques can then be used to reduce the problem dimension. In this investigation, the stiffness matrix is formulated using the general continuum mechanics approach and the strain split method is used in order to alleviate the locking problem in the case of beam and plate elements. The frequencies and mode shapes predicted using the spatial ANCF/FFR elements are compared to those obtained using a commercial FE code and analytical solutions. It is shown that the strain split method is a viable locking alleviation technique, and when it is used to formulate the stiffness matrix, the resulting frequencies agree well with the analytical and the FE-code reference solutions. The new ANCF/FFR elements have the same number of nodal coordinates as their counterpart conventional finite elements. Furthermore, when using the ANCF/FFR elements, no distinction is made between plate and shell elements.

While the recently introduced spatial elements considered in this study can be used to develop geometrically accurate reduced-order models for structural and MBS applications, more research is needed in order to understand their behavior and improve their performance and convergence characteristics. To this end, different formulations of the elastic forces can be attempted as well as different new locking-alleviation techniques more suited for these elements can be developed. In MBS applications, these elements can be used with the nonlinear FFR formulation to create a local linear problem that allows utilizing coordinate reduction techniques. In MBS applications, only the shape of deformations is important since the frequencies of the linear problem does not have an effect on the solution of the nonlinear problem [54]. Therefore, the frequency convergence can be more important in structural system applications as compared to MBS applications. Furthermore, use of linearization or perturbation techniques to study stability of MBS applications based on the constant mass and stiffness matrices of these elements or other conventional elements is not recommended because of the problems associated with such linearization and perturbation techniques when applied to the highly nonlinear MBS applications [55,56].

References

[1] Bathe, K. J., 1996, *Finite Element Procedures*, Prentice Hall, Englewood Cliffs, NJ.
[2] Belytschko, T., Liu, W. K., and Moran, B., 2000, *Nonlinear Finite Elements for Continua and Structures*, Wiley, New York.
[3] Bonet, J., and Wood, R. D., 1997, *Nonlinear Continuum Mechanics for Finite Element Analysis*, Cambridge University Press, Cambridge, UK.
[4] Cook, R. D., Malkus, D. S., and Plesha, M. E., 1989, *Concepts and Applications of Finite Element Analysis*, 3rd ed., Wiley, Hoboken, NJ.
[5] Crisfield, M. A., 1991, *Nonlinear Finite Element Analysis of Solids and Structures: Essentials*, Vol. 1, Wiley, Hoboken, NJ.
[6] Zienkiewicz, O. C., 1977, *The Finite Element Method*, 3rd ed., McGraw-Hill, New York.

[7] Zienkiewicz, O. C., and Taylor, R. L., 2000, *The Finite Element Method, Vol. 2: Solid Mechanics*, 5th ed., Butterworth Heinemann, Oxford, UK.

[8] Piegl, L., and Tiller, W., 1997, *The NURBS Book*, 2nd ed., Springer, New York.

[9] Goldenweizer, A., 1961, *Theory of Thin Elastic Shells*, Pergamon Press, Oxford, UK.

[10] Kratzig, W. B., and Onate, E., eds., 1990, *Computational Mechanics of Nonlinear Response of Shells*, Springer-Verlag, New York.

[11] Naghdi, P. M., 1972, "The Theory of Shells and Plates," Handb. Der Phys., **6**(a/2), pp. 425–640.

[12] Noor, A. K., 1990, "Bibliography of Monographs and Surveys on Shells," ASME Appl. Mech. Rev., **43**(9), pp. 223–234.

[13] A. K., Noor, T. Belytschko, and J. C. Simo, eds., 1989, *Analytical and Computational Models of Shells*, Vol. 3, ASME CED, New York.

[14] Reddy, J. N., 2007, *Theory and Analysis of Elastic Plates and Shells*, 2nd ed., CRC Press, Boca Raton, FL.

[15] Specht, B., 1988, "Modified Shape Functions for the Three-Node Plate Bending Element Passing the Patch Test," Int. J. Numer. Methods Eng., **26**(3), pp. 705–715.

[16] Stolarski, H., Belytschko, T., and Lee, S. H., 1995, "A Review of Shell Finite Elements and Corotational Theories," Comput. Mech. Adv., **2**(2), pp. 125–212.

[17] Ugural, A. C., 1981, *Stresses in Plates and Shells*, McGraw-Hill, New York.

[18] Mackenzie, D., 2011, "Curing Ill Surfaces," SIAM News, **44**, pp. 1–12.

[19] Shabana, A. A., 2016, "ANCF Consistent Rotation-Based Finite Element Formulation," ASME J. Comput. Nonlinear Dyn., **11**(1), p. 014502.

[20] Zheng, Y., and Shabana, A. A., 2017, "A Two-Dimensional Shear Deformable ANCF Consistent Rotation-Based Formulation Beam Element," Nonlinear Dyn., **87**(2), pp. 1031–1043.

[21] Shabana, A. A., 2018, "Geometrically Accurate Infinitesimal-Rotation Spatial Finite Elements," Proc. Inst. Mech. Eng., Part K, **233**(1), pp. 182–187.

[22] Amabili, M., Sarkar, A., and PaiDoussis, M. P., 2003, "Reduced-Order Models for Nonlinear Vibrations of Cylindrical Shells Via the Proper Orthogonal Decomposition Method," J. Fluids Struct., **18**(2), pp. 227–250.

[23] Craig, R. R., Jr., 1983, *Structural Dynamics: An Introduction to Computer Methods*, 1st ed., Wiley, New York.

[24] Craig, R. R., Jr., and Bampton, M. C. C., 1968, "Coupling of Substructures for Dynamic Analyses," AIAA J., **6**(7), pp. 1313–1319.

[25] Epureanu, B. I., 2003, "A Parametric Analysis of Reduced Order Models of Viscous Flows in Turbomachinery," J. Fluids Struct., **17**(7), pp. 971–982.

[26] Fehr, J., and Eberhard, P., 2011, "Simulation Process of Flexible Multibody Systems With Non-Modal Model Order Reduction Techniques," Multibody Syst. Dyn., **25**(3), pp. 313–334.

[27] Fischer, M., and Eberhard, P., 2014, "Linear Model Reduction of Large Scale Industrial Models in Elastic Multibody Dynamics," Multibody Syst. Dyn., **31**(1), pp. 27–46.

[28] Flanigan, C. C., 1991, "Development of the IRS Component Dynamic Reduction Method for Substructure Analysis," AIAA Paper No. 1991-1056.

[29] Guyan, R. J., 1965, "Reduction of Stiffness and Mass Matrices," AIAA J., **3**(2), p. 380.

[30] Kerschen, G., Golinval, J. C., Vakakis, A. F., and Bergman, L. A., 2005, "The Method of Proper Orthogonal Decomposition for Dynamical Characterization and Order Reduction of Mechanical Systems: An Overview," Nonlinear Dyn., **41**(1–3), pp. 147–169.

[31] Madden, A., Castanier, M. P., and Epureanu, B. I., 2008, "Reduced-Order Model Construction Procedure for Robust Mistuning Identification of Blisks," AIAA J., **46**(11), pp. 2890–2898.

[32] Mordfin, T. G., 1995, "Articulating Flexible Multibody Dynamics, Substructure Synthesis and Finite Elements," Adv. Astronaut. Sci., **89**, pp. 1097–1116.

[33] Mottershead, J., and Friswell, M. I., 1993, "Model Updating in Structural Dynamics; a Survey," J. Sound Vib., **167**(2), pp. 347–375.

[34] Wu, L., and Tiso, P., 2016, "Nonlinear Model Order Reduction for Flexible Multibody Dynamics: A Modal Derivatives Approach," Multibody Syst. Dyn., **36**(4), pp. 405–425.

[35] Shabana, A. A., 2013, *Dynamics of Multibody Systems*, 4th ed., Cambridge University Press, Cambridge, UK.

[36] Shabana, A. A., 2018, *Computational Continuum Mechanics*, 3rd ed., Wiley & Sons, Chichester, UK.

[37] Shabana, A. A., 2017, "Geometrically Accurate Floating Frame of Reference Finite Elements for the Small Deformation Problem," Proc. Inst. Mech. Eng., Part K, **232**(2), pp. 286–292.

[38] Goldstein, H., 1950, *Classical Mechanics*, Addison-Wesley, Boston, MA.

[39] Greenwood, D. T., 1988, *Principles of Dynamics*, Prentice Hall, Upper Saddle River, NJ.

[40] Roberson, R. E., and Schwertassek, R., 1988, *Dynamics of Multibody Systems*, Springer-Verlag, Berlin.

[41] Ogden, R. W., 1984, *Non-Linear Elastic Deformations*, Dover Publications, Mineola, NY.

[42] Yakoub, R. Y., and Shabana, A. A., 2001, "Three-Dimensional Absolute Nodal Coordinate Formulation for Beam Elements: Implementation and Applications," Trans. ASME J. Mech. Des., **123**(4), pp. 614–621.

[43] Mikkola, A. M., and Shabana, A. A., 2003, "A Non-Incremental Finite Element Procedure for the Analysis of Large Deformation of Plates and Shells in Mechanical System Applications," Multibody Syst. Dyn., **9**(3), pp. 283–309.

[44] Olshevskiy, A., Dmitrochenko, O., and Kim, C. W., 2014, "Three-Dimensional Solid Brick Element Using Slopes in the Absolute Nodal Coordinate Formulation," ASME J. Comput. Nonlinear Dyn., **9**(2), p. 021001.

[45] Patel, M., and Shabana, A. A., 2018, "Locking Alleviation in the Large Displacement Analysis of Beam Elements: The Strain Split Method," Acta Mech., **229**(7), pp. 2923–2946.

[46] Berzeri, M., and Shabana, A. A., 2000, "Development of Simple Models for the Elastic Forces in the Absolute Nodal Coordinate Formulation," J. Sound Vib., **235**(4), pp. 539–565.

[47] Gerstmayr, J., and Shabana, A. A., 2006, "Analysis of Thin Beams and Cables Using the Absolute Nodal Coordinate Formulation," Nonlinear Dyn., **45**(1–2), pp. 109–130.

[48] Gerstmayr, J., Matikainen, M. K., and Mikkola, A. M., 2008, "A Geometrically Exact Beam Element Based on the Absolute Nodal Coordinate Formulation," Multibody Syst. Dyn., **20**(4), pp. 359–384.

[49] Nachbagauer, K., 2014, "State of the Art of ANCF Elements Regarding Geometric Description, Interpolation Strategies, Definition of Elastic Forces, Validation and the Locking Phenomenon in Comparison With Proposed Beam Finite Elements," Arch. Comput. Methods Eng., **21**(3), pp. 293–319.

[50] Bathe, K. J., and Dvorkin, E. N., 1985, "A Four-Node Plate Bending Element Based on Mindlin/Reissner Plate Theory and a Mixed Interpolation," Int. J. Numer. Methods Eng., **21**(2), pp. 367–383.

[51] Bathe, K. J., and Dvorkin, E. N., 1986, "A Formulation of General Shell Elements—The Use Mixed Interpolation of Tensorial Components," Int. J. Numer. Methods Eng., **22**(3), pp. 697–722.

[52] Timoshenko, S. P., 1955, *Vibration Problems in Engineering*, McGraw-Hill, New York.

[53] Shabana, A. A., Desai, C. J., Grossi, E., and Patel, M., 2020, "Generalization of the Strain-Split Method and Evaluation of the Nonlinear ANCF Finite Elements," Acta Mech., **231**(4), pp. 1365–1376.

[54] Shabana, A. A., 1996, "Resonance Conditions and Deformable Body Coordinate Systems," J. Sound Vib., **192**(1), pp. 389–398.

[55] Shabana, A. A., 2010, "On the Definition of the Natural Frequency of Oscillations in Nonlinear Large Rotation Problems," J. Sound Vib., **329**(15), pp. 3171–3181.

[56] Shabana, A. A., Zaher, M. H., Recuero, A. M., and Rathod, C., 2011, "Study of Nonlinear System Stability Using Eigenvalue Analysis: Gyroscopic Motion," Sound Vib., **330**(24), pp. 6006–6022.